Check for updates

JGR Atmospheres

RESEARCH ARTICLE
10.1029/2024JD041677

A Climatological Study of the Frequency Spectra of Vertical Winds From MU Radar Data (1987–2022)

Hubert Luce[1], **Noriyuki Nishi**[2], **and Hiroyuki Hashiguchi**[1]

[1]Research Institute for Sustainable Humanosphere, Kyoto University, Kyoto, Japan, [2]Faculty of Science, Fukuoka University, Fukuoka, Japan

Key Points:

- Frequency spectra of vertical velocity show very distinct features in the troposphere and stratosphere
- The characteristics of the frequency spectra of W are not consistent with the existing gravity wave theories

Correspondence to:

H. Luce,
luce@rish.kyoto-u.ac.jp

Citation:

Luce, H., Nishi, N., & Hashiguchi, H. (2024). A climatological study of the frequency spectra of vertical winds from MU radar data (1987–2022). *Journal of Geophysical Research: Atmospheres*, *129*, e2024JD041677. https://doi.org/10.1029/2024JD041677

Received 25 MAY 2024
Accepted 5 NOV 2024

Author Contributions:

Conceptualization: Hubert Luce, Noriyuki Nishi, Hiroyuki Hashiguchi
Data curation: Hiroyuki Hashiguchi
Formal analysis: Hubert Luce
Investigation: Hubert Luce, Noriyuki Nishi, Hiroyuki Hashiguchi
Methodology: Hubert Luce, Hiroyuki Hashiguchi
Resources: Hiroyuki Hashiguchi
Software: Hubert Luce
Supervision: Hubert Luce
Validation: Hubert Luce, Noriyuki Nishi, Hiroyuki Hashiguchi
Writing – original draft: Hubert Luce, Noriyuki Nishi, Hiroyuki Hashiguchi
Writing – review & editing: Hubert Luce, Noriyuki Nishi, Hiroyuki Hashiguchi

© 2024. The Author(s).
This is an open access article under the terms of the Creative Commons Attribution-NonCommercial-NoDerivs License, which permits use and distribution in any medium, provided the original work is properly cited, the use is non-commercial and no modifications or adaptations are made.

Abstract

In this paper, we present a statistical analysis of the frequency spectra of vertical velocity W based on data collected by the VHF middle and upper atmosphere (MU) radar from 2.025 to 19.875 km altitude during several days per month over 36 years (1987–2022). We analyzed the mean spectral slopes S_W in the band [0.5–6 hr], which is in the core of the period range for internal gravity waves at the MU radar latitude (~36° N). First, we tested the performance of several spectral estimators when data are missing to minimize estimation bias on S_W and variance. Second, we analyzed the properties of S_W. We found a dependence on radar echo power aspect ratio and power imbalance between oblique beams maybe due to contaminations of W measurements by the horizontal wind U. After corrections, we found that: (a) S_W in the troposphere ($N^2 < 2 \times 10^{-4}$ rad^{2}s^{-2}) is almost seasonally invariant (~−0.8) despite the strong variability of U and (b) S_W is highly variable in the stratosphere ($N^2 > 2 \times 10^{-4}$ rad^{2}s^{-2}) from ~0 to −1.2 and shows a clear exponential dependence on U at least up to 70 ms^{-1}. An empirical expression of the apparent frequency spectra in the stratosphere is $\sim\omega^{\alpha \ln (U - U_{\min})}$ with, for example, $\alpha \sim -0.27$ and $U_{\min} \sim 3.5$ ms^{-1}. From numerical simulations, we show that Doppler shift effects cannot explain the dependence on U. Therefore, the variation of S_W with U may represent a real change in the shape of the intrinsic frequency spectrum, which is not considered in the theoretical models.

Plain Language Summary

Frequency power spectral densities (or frequency spectra) of vertical air velocity W can provide information about the properties of internal gravity waves in the atmosphere. In the present work, they are estimated from time series of W collected from the VHF middle and upper atmosphere (MU) radar in the troposphere and lower stratosphere. For the first time, we quantify several possible processing and instrumental biases that may affect the estimates of the slope and variance of the frequency spectra in the range [0.5–6] hours. In light of these results, we analyzed the monthly variability in the spectral slopes. We found a small seasonal variability in the troposphere (~−0.8) despite a strong variability of the horizontal wind speed U. In contrast, the spectral slope shows a strong dependence on U in the stratosphere. This dependence is qualitatively, but not quantitatively, consistent with the expected effects of Doppler shifting (which produces an apparent frequency for a fixed observer). Further studies are needed to explain the difference with the theoretical models of gravity waves.

1. Introduction

The study of mesoscale motions in the atmosphere is necessary to understand the interactions between large and small scale motions. In particular, the study of the vertical motions produced by gravity waves and convection and their role in meteorological systems is of paramount importance. It is part of the mission of the European/Japanese EarthCARE satellite very recently place in orbit (May 2024), which carries instruments for the characterization of clouds and aerosols and for radiation measurements (e.g., Wehr et al., 2023). The atmospheric motions are generally described in terms of frequency and wavenumber power spectral densities (or spectra for short). There is a relative consensus for horizontal frequency spectra of horizontal winds U associated with mesoscale or synoptic motions: they exhibit a ω^{-p} law with $\frac{5}{3} \leq p \leq 2$. The internal oceanic gravity wave (IGW) model of Garrett and Munk (1975), adapted to atmospheric IGWs by VanZandt (1982), predicts $p = 2$. The saturated-cascade similitude theory of Dewan (1997), which combines gravity wave saturation and a Kolmogorov turbulence-like wave cascade predicts the same slope. On the other hand, the inverse cascade theory of 2-D mesoscale turbulence predicts $p = 5/3$ (e.g., Lilly, 1983). The small difference between the spectral slopes predicted by the different theories makes them difficult to verify experimentally, as measurements are often subject to uncertainties and biases (e.g., Hocking et al., 2021). For this reason, several authors suggested to study the spectral properties of vertical winds W (e.g., Ecklund et al., 1985; Ghosh et al., 2022; Larsen et al., 1986, 1987; Li et al., 2018;

21698996, 2024, 23, Downloaded from https://agupubs.onlinelibrary.wiley.com/doi/10.1029/2024JD041677 by Cochrane Japan, Wiley Online Library on [19/01/2025]. See the Terms and Conditions (https://onlinelibrary.wiley.com/terms-and-conditions) on Wiley Online Library for rules of use; OA articles are governed by the applicable Creative Commons License

Muschinski et al., 2001; VanZandt et al., 1991; Yamamoto et al., 1996). The studies show much more variable characteristics of the W spectra. For weak horizontal and vertical winds, Ecklund et al. (1985) showed nearly flat frequency spectra ($p \sim 0$) for periods of the order of [15 min–1 few hr] and a rapid decrease for periods smaller than the Brünt-Vaisala (BV) period. These properties are consistent with the Garrett and Munk model of IGW, as $p = 0$ is expected for $f \leq \omega \leq N$ where f is the inertial frequency and N is the BV frequency. During periods of strong wind, Ecklund et al. reported frequency spectra of W with levels increased by 1–2 orders of magnitude and $p \sim 5/3$ with no clear spectral drop above N. Ecklund et al. (1986) made a preliminary climatological study and found $p \sim 1$ for general conditions, a statistical value confirmed by Larsen et al. (1986). Using 15 days of VHF SOUSY radar data, Larsen et al. (1987) reported that p decreases with height from ~ 1 to $p \sim 1/2$ in the stratosphere. Using 15 days of data collected from the same radar, Muschinski et al. (2001) found $p \sim 5/3$ in the lower troposphere. Using 3 days of data with the MU radar, Yamamoto et al. (1996) found $p \sim 0.4$ on average (value derived from their Table 3). Using 4 years of data with the MAARSY radar, Li et al. (2018) found p from $1/3$ to $5/3$ up to horizontal winds of 10 ms^{-1} and then almost constant slopes ($p \sim 5/3$) for stronger winds. Using 4 years of data with the same radar, Ghosh et al. (2022) reported $0 < p < 1$ and a decrease with height.

The greater variability in the slopes of W spectra may a priori be due to several factors. First, when associated with gravity wave motions, the spectra of gravity waves are subject to Doppler shift (e.g., Scheffler & Liu, 1985, 1986). A ground-based radar measures an apparent (Eulerian) frequency spectrum that is upshifted or downshifted by the horizontal wind, depending on the direction of $\vec{U}$ with respect to the direction of the wavenumber vector $\vec{k}$. The Doppler shift causes a broadening of the frequency spectrum, which explains the IGW energies at frequencies smaller than f and larger than N in the observed spectra, especially when the horizontal wind is strong. Note that (2-D or Kolmogorov) turbulence is not subject to Doppler shift within the Taylor frozen turbulence advection hypothesis (so that $\omega = kU$). Of course, the Doppler shift also applies to the frequency spectra of horizontal winds. Therefore, it cannot be the sole factor. Second, the estimation of frequency spectra of W from radar data may be subject to processing and measurement biases inherent in the radar technique and performance (e.g., Hocking et al., 2016; Muschinski, 1996).

We first assessed the impact of missing data on the evaluation of spectra using several methods. Several spectral estimators proposed in the literature were tested. Based on the results of this analysis, we applied a data rejection criterion that allowed us to neglect the impact of missing data in the interpretation of the spectra. Since W can be several orders of magnitude smaller than U, contamination of W measurements by horizontal winds can occur for several reasons, for example, misalignment of the vertical beam (Huaman & Balsley, 1996), depointing of a truly vertical beam due to tilted anisotropic scattering layers (Muschinski, 1996). The latter case is responsible for the power imbalance between symmetric oblique beams, especially when the aspect ratio, defined as the ratio between the echo power at vertical and oblique incidence, is increased (a possible signature of specular or diffuse reflection or Fresnel scattering). Our analysis shows for the first time an effect of aspect ratio and power imbalance on the slopes of the frequency spectra. This effect can be comparable in magnitude to the Doppler shift. Taking these different factors into account should allow a more reliable comparison of W spectra with theoretical spectra.

The paper is organized as follows. First, the MU radar data set collected for long-term routine monitoring and the data availability are briefly described in Section 2. The methodology and performance tests of various methods used to compute the frequency spectra of W from time series including missing data are described in Section 3. The results of the analysis and the interpretation of the spectral slopes in terms of Doppler shifting and other biases are discussed in Section 4. Finally, a summary is given in Section 5.

2. Description of the MU Radar Data

The MU radar is a 46.5-MHz system built in 1984 at Shigaraki, Japan (34.85°N, 136.10°) (Fukao et al., 1985). Data are collected every month for a few consecutive days (typically 5 days) in a routine observation mode described in Table 1. The data have been processed and archived since March 1986. The files contain radar echo powers, radial winds, and spectral widths in five directions (vertical, north, east, south, and west 10° off zenith) with a time resolution of 10 min from the range of 2.025–19.875 km and a range resolution of 150 m. The radar beam width, defined as the two-way half-power full width, is 3.6°. The horizontal distance between the centers of the radar volumes in symmetrical beams is 0.7 km (6.9 km) at 2.025 (19.875) km. Our study focuses on vertical velocity measurements. In addition to the direct vertical measurement W, the beam configuration can provide

21698996, 2024, 23, Downloaded from https://agupubs.onlinelibrary.wiley.com/doi/10.1029/2024JD041677 by Cochrane Japan, Wiley Online Library on [19/01/2025]. See the Terms and Conditions (https://onlinelibrary.wiley.com/terms-and-conditions) on Wiley Online Library for rules of use; OA articles are governed by the applicable Creative Commons License

Table 1
MU Radar Observation Parameters

Parameter	Value (before August 2005)	Value (before September 2005)
Sub pulse length	1 μ sec	1 μ sec
Inter Pulse Period	400 μ sec	400 μ sec
Number of coherent integrations	38	32
Number of incoherent integrations	5 (TR Mode)/6 (ST Mode)	7
Number of FFT data	128	128
Pulse compression	1 bit (TR Mode)/16 bit complementary code (ST Mode)	16 bit optimal code

Note. TR = Troposphere, ST = Stratosphere.

two additional independent estimates from the expressions $W_{\mathrm{NS}} = (V_N + V_S)/(2\cos(10°))$ and $W_{\mathrm{EW}} = (V_E + V_W)/(2\cos(10°))$, where V_N, V_S, V_E, and V_W are the radial velocities from the north, south, east, and west beams, respectively.

In the present work, we use 36 years of data from January 1987 to December 2022. In September 2005, the radar was upgraded with more capabilities, improved performance, and a different pulse compression (Hassenpflug et al., 2008) without affecting the accuracy of the Doppler measurements. Each period of each month was divided into an integer number of 1-day segments (corresponding to 144 time series data if no data are missing as the time resolution is 10 min) shifted by half a day in order to compute the frequency spectra. The oversampling by a factor of two is justified by the method of calculating the spectra described in Section 3. The left panel of Figure 1 shows the total number of one-day W, W_{NS}, and W_{EW} time series per month. It is about 30,000, that is, ∼250 for each of the 120 sampled heights. The larger number of 1-day time series in January and December is due to the longer observation period in these 2 months. Many time series have missing data due to several factors: mainly too low signal-to-noise ratio (SNR), ground clutter echoes, precipitation echoes, aircraft echoes, external electromagnetic interference, and/or temporary shutdown. As the missing data can affect the frequency spectra, their processing is described in detail in Section 3. Of the W (W_{NS}, W_{EW}) time series, ∼70%–90% (∼50%–60%) have less than 15% of missing data and ∼20%–30% (∼10%–20%) have no missing data (right panels of Figure 1). There is a very pronounced difference in availability between W and (W_{NS}, W_{EW}) due to a better SNR at vertical incidence. In the following, TS85 and TS100 will refer to time series with less than 15% of missing data and no gaps, respectively. TS85 distributions are shown because a maximum of 15% missing data was found to be a necessary condition to minimize the biases in the spectral estimates (slope and variance) for all the methods (see Section 3). The representation in % shows a maximum availability in spring (April, May, and June) particularly pronounced for W_{NS} and W_{EW}. This characteristic is due to a better SNR in the upper troposphere because of the increased turbulence during spring (not shown, this observation will be detailed in a later study). Figure 2 shows the percentage of TS100 (black) and TS85 (gray) as a function of altitude for W (top), W_{NS}, (middle), and W_{EW} (bottom) for the whole period 1987–2022. Below 5.32 km altitude, the data availability for the three parameters is artificially reduced because the observations started at 5.32 km altitude during daytime (08:00-16:00 LT) until June 1989. A narrow minimum is observed just above 6.0 km altitude due to the sporadic presence of ground clutter. The percentage of $TS85(W)$ remains above 70% up to ∼18.5 km and rapidly drops to ∼40% at the highest altitudes due to SNR degradation. The minimum of $TS85(W)$ around 13 km is mainly due to the minimum of echoes received below the tropopause in summer. The percentage of $TS100(W)$ is about 10% above 10 km. The percentage of TS85 (W_{NS} , W_{EW}) drops rapidly from ∼90% at 8 km to ∼20–30% at 14 km and then tends to stabilize up to 16 km before dropping to 5% at the top. This characteristic can be explained by the frequent occurrence of ground clutter, which affects the oblique directions in the altitude range (∼13–16 km). However, overall, except near the top, a large amount of data is available for spectral analysis.

3. Methodology

3.1. PSD (Spectrum) Calculation

The 144 time series data are first detrended by applying a linear fit. They are weighted by a (variance preserved) Hanning window. Because of the loss of energy at the edges of the time series, an oversampling factor of two is

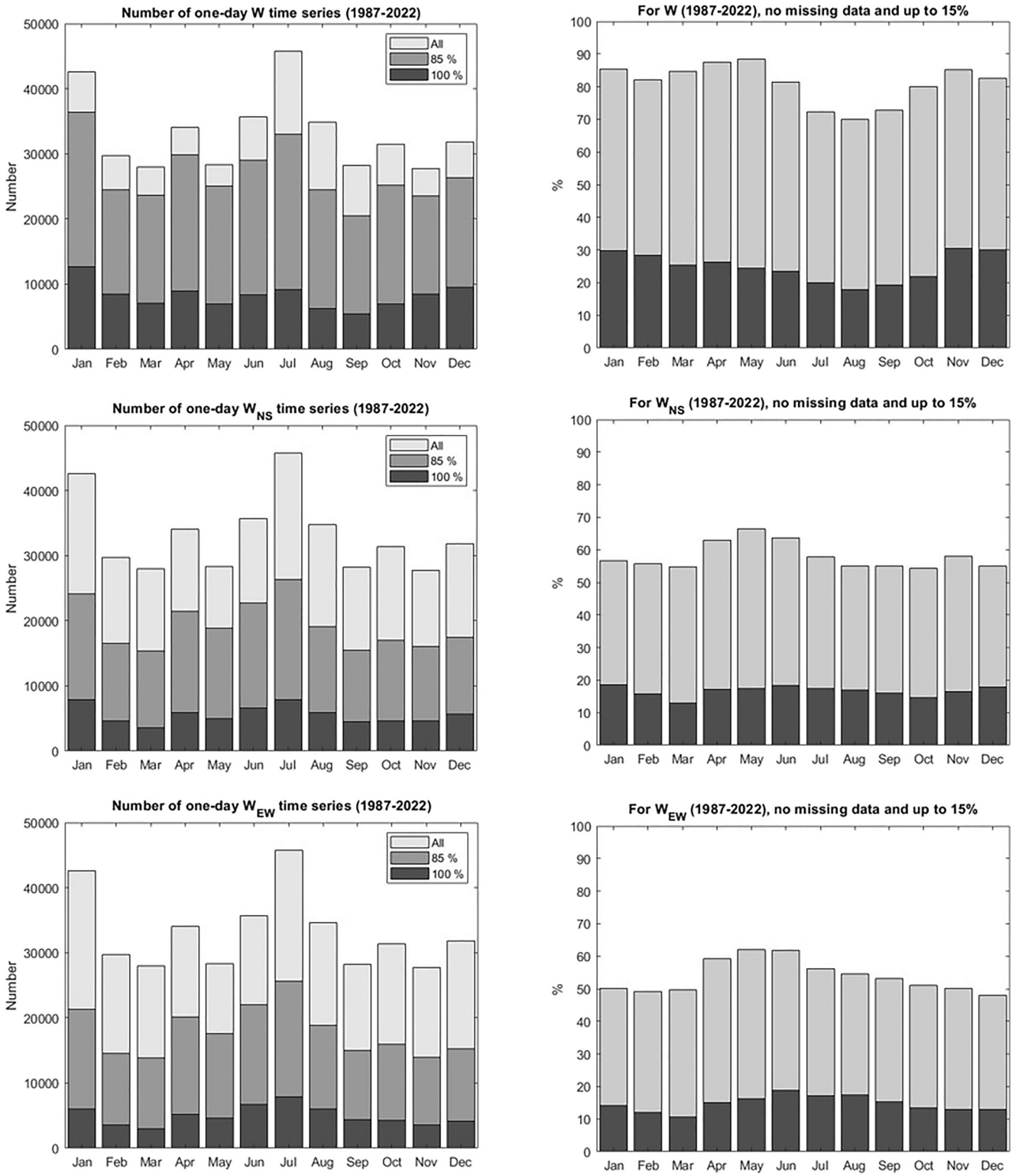

Figure 1. (Left) Light gray: Total number of available time series with a length of 144 data (i.e., 1 day with a time resolution of 10 min) for each month and the period 1987–2022. Dark gray: Number of time series with less than 15% missing data. Black: Number of time series with no missing data for W (top), W_{NS} (middle), and W_{EW} (bottom). (Right) The corresponding percentage of time series.

21698996, 2024, 23, Downloaded from https://agupubs.onlinelibrary.wiley.com/doi/10.1029/2024JD041677 by Cochrane Japan, Wiley Online Library on [19/01/2025]. See the Terms and Conditions (https://onlinelibrary.wiley.com/terms-and-conditions) on Wiley Online Library for rules of use; OA articles are governed by the applicable Creative Commons License

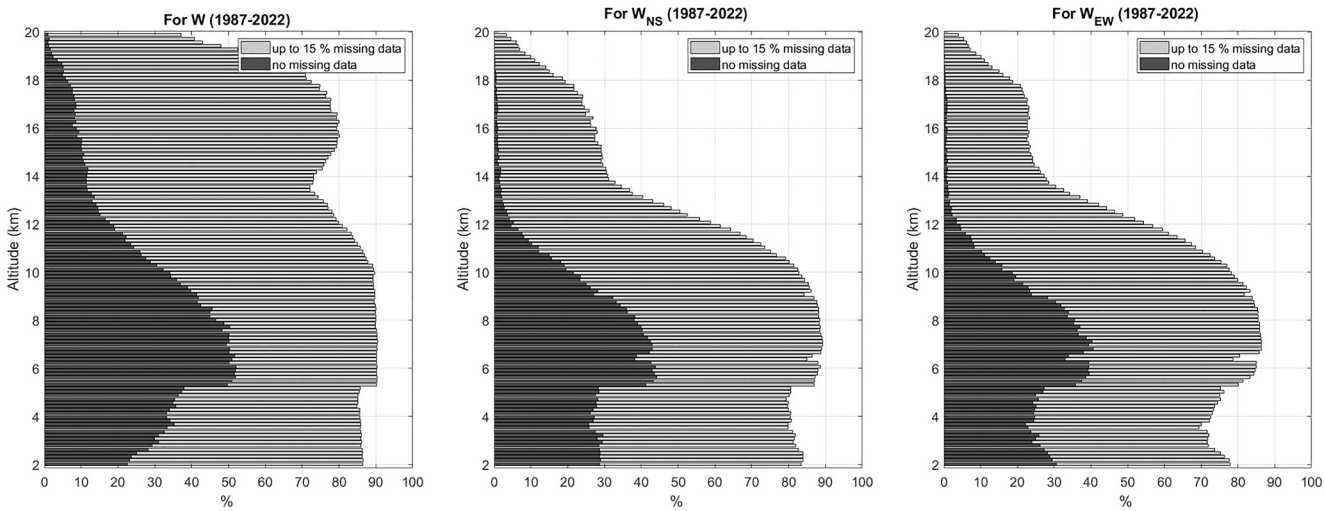

Figure 2. Percentage of time series with a length of 144 data (i.e., 1 day with a time resolution of 10 min) without missing data (black) for W (top), W_{NS} (middle), and W_{EW} (bottom) data and up to 15% (gray) versus altitude for the period 1987–2022.

applied, that is, the 1-day time series are extracted every 12 hr. The frequency spectra are first calculated using processing methods described in Section 3.2. With a time sampling of 600 s, the Nyquist frequency is 8.33×10^{-4} Hz or 3 cy hr^{-1}. The spectral slopes, hereafter noted S_W, in the band [0.5–6 hr] (or [0.167–2.00] cy hr^{-1}) are then obtained by (a) dividing the spectral band into two equal sub-bands (in log scale), (b) calculating the variance for each sub-band, and (c) determining the slope S_W of the straight line passing through these two points. This procedure allows us to estimate the variance in the band at the same time. A graphical description of the method can be found for another application in Figure 1 of Luce et al. (2019).

3.2. Processing of Time Series With Missing Data

Obviously, the more data that are missing, the more the spectral estimates are affected. The effect also depends on how the missing data are distributed. As explained above, the causes of data gaps can be multiple and have different characteristics. We consider two extreme cases:

1. The position of the missing data is randomly distributed. This is the case when the data gaps are due to, for example, low SNR or aircraft echoes or any sporadic interference lasting less than 10 min or so.
2. The missing data are all consecutive (e.g., a data gap of a few hours). This is the case when there are, for example, ground clutter echoes, electromagnetic interference, rain echoes, or temporary shutdowns.

In practice, (1) and (2), hereafter referred to as RMD (random missing data) and CMD (consecutive missing data), respectively, are often mixed. For a given percentage of missing data, the results for mixed conditions are expected to be intermediate between RMD and CMD.

Examples of W time series of 144 data without gaps and for RMD and CMD are shown in Figure 3a. To assess the effect of missing data in the measured time series on S_W and the variance, we first arbitrarily selected 10,000 series without data gaps. We then calculated spectra S_W and variances using the method described in Section 3.1. Next, we removed data to simulate RMD and CMD from 1% to 30% with a step of 1%. Finally, we considered four methods to fill in the gaps or deal with the missing data. Namely:

1. A linear interpolation to fill in the gaps for each 1-day segment independently. If there are missing data at the edges of the time series, they are replaced by 0. The method is hereafter referred to as FFT-LI.
2. A replacement of the missing data by the mean (or median) value of the time series (with gaps). The method is hereafter referred to as FFT-MV. This method is not a priori acceptable when time series are dominated by low-frequency components (as in the case of horizontal wind), as it can generate artificial peaks and spurious high-frequency levels.

21698996, 2024, 23, Downloaded from https://agupubs.onlinelibrary.wiley.com/doi/10.1029/2024JD041677 by Cochrane Japan, Wiley Online Library on [19/01/2025]. See the Terms and Conditions (https://onlinelibrary.wiley.com/terms-and-conditions) on Wiley Online Library for rules of use; OA articles are governed by the applicable Creative Commons License

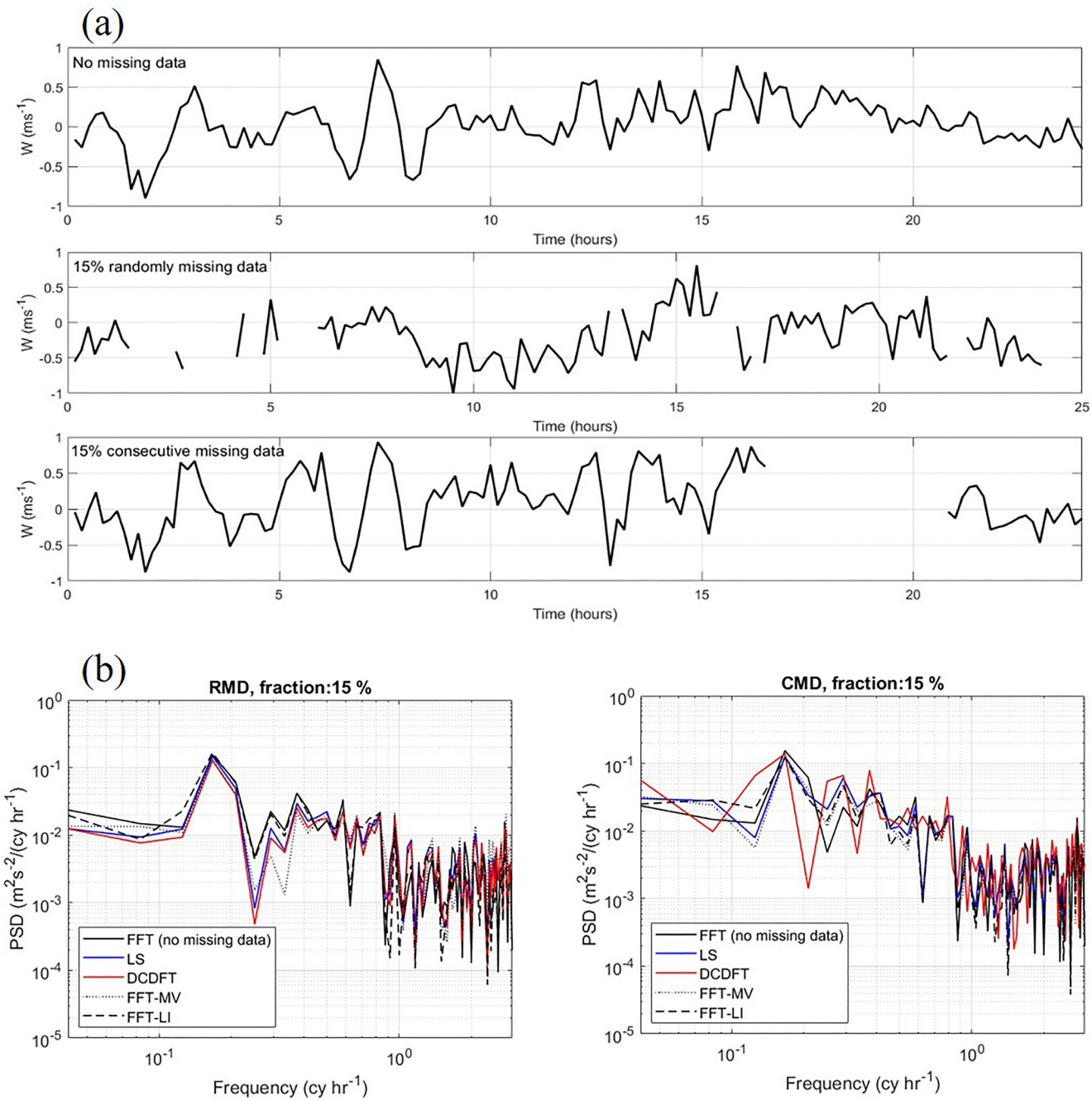

Figure 3. (a) Examples of time series (144 data) of W (top) with no data gaps, (middle) with random missing data (RMD) (15%), and (bottom) with 15% consecutive missing data (CMD). (b) Examples of frequency spectra obtained with RMD (left) and CMD (right) using FFT (before data removal), LS, DCDFT, FFT-MV, and FFT-LI. The same original time series are used in both cases.

3. The Lomb-Scargle (LS) spectral estimator (Lomb, 1976; Scargle, 1982) designed for unevenly sampled data sets. It was used by Li et al. (2018) for W data collected with the MAARSY radar for the same purpose. The authors describe the principle and the equations of LS. Zhan et al. (1996) tested LS for estimating horizontal wind spectra measured at mesospheric heights.
4. The date-compensated discrete Fourier transform (DCDFT) spectral estimator (Ferraz-Mello, 1981), also applied to time series with unevenly spaced observations, was used by Hocking et al. (2021) for data collected with a network of wind profilers.

21698996, 2024, 23, Downloaded from https://agupubs.onlinelibrary.wiley.com/doi/10.1029/2024JD041677 by Cochrane Japan, Wiley Online Library on [19/01/2025]. See the Terms and Conditions (https://onlinelibrary.wiley.com/terms-and-conditions) on Wiley Online Library for rules of use; OA articles are governed by the applicable Creative Commons License

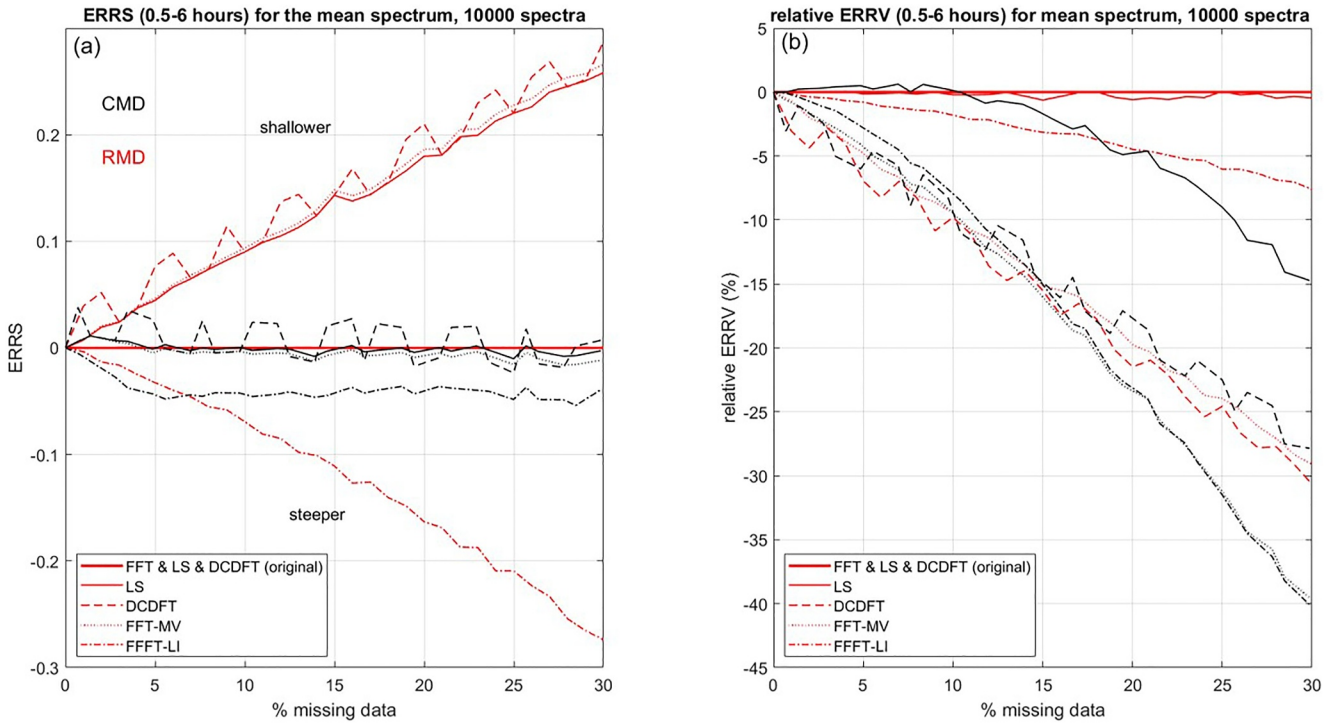

Figure 4. (a) Absolute error on the spectral slope (ERRS) in the period range [0.5–6.0 hr] versus % of missing data for CMD (black) and RMD (red) using LS (solid), DCDFT (dashed), FFT-MV (dotted), and FFT-LI (dashed dotted). (b) Same as (a) for the relative error on the variance (ERRV) in the same period range [0.5–6.0 hr].

LS and DCDFT use time series as they are. LS and DCDFT without missing data give the same results as FFT. Figure 3b shows examples of spectra obtained from a 144 time series data using all the spectral estimators for the RMD (left) and CMD (right) cases for 15% missing data. The spectra without missing data obtained by FFT, LS, and DCDFT are shown by the single black solid curve. It can be seen that the largest differences between the spectra are at the lowest frequencies and for CMD.

To compare the statistical performance between the methods, we calculated 10,000 spectra using FFT-LI, FFT-MV, LS, and DCDFT for both RMD and CMD cases. We then calculated the mean spectrum, S_W and variance for the period [0.5–6 hr] and finally the absolute error relative to the spectral slope (ERRS) and the relative error relative to the variance (ERRV). ERRS is defined as the difference between S_W without missing data and S_W with data gaps. The absolute error on the variance is calculated in the same way, and ERRV is obtained by dividing by the variance (in the same frequency band) of the original time series. The aim is to find out the percentage of missing data that are allowed in the time series when we set a threshold for ERRS and ERRV not to be exceeded for both RMD and CMD. We found that the results are not significantly different if we use an arithmetic or geometric mean of the spectra and if we first calculate S_W for each spectrum and then average them. Therefore, only one option is shown in Figure 4.

Figures 4a and 4b show ERRS and ERRV for RMD (red lines) and CMD (black lines), respectively, as a function of percentage of missing data (0%–30%). The results using LS, DCDFT, FFT-MV, and FFT-LI are shown as solid, dashed, dotted, and dotted-dashed lines, respectively. By definition, ERRS $= 0$ and ERRV $= 0$ for all the methods with the original time series without data gaps (thick red solid lines). When ERRS > 0, then the estimated slope is flatter. For example, if S_W without data gaps is -1 and ERRS $= +0.1$, then the estimated slope is -0.9. When ERRS < 0, then the estimated slope is steeper. For example, if S_W without data gaps is -1 and $= -0.1$, then the estimated slope is -1.1. As the purpose is only to identify the best method for a given tolerance on ERRS and ERRV, we will not describe the results in detail.

The characteristics of ERRS differ between CMD and RMD. For CMD, ERRS for all the methods is independent of the percentage of missing data after a few % and at least up to 30%. It is negligible ($\sim$0) for LS, DCDFT and FFT-MV and ~ -0.04 for FFT-LI. DCDFT produces small oscillations for all results. For RMD, LS, DCDFT, and FFT-

21698996, 2024, 23, Downloaded from https://agupubs.onlinelibrary.wiley.com/doi/10.1029/2024JD041677 by Cochrane Japan, Wiley Online Library on [19/01/2025]. See the Terms and Conditions (https://onlinelibrary.wiley.com/terms-and-conditions) on Wiley Online Library for rules of use; OA articles are governed by the applicable Creative Commons License

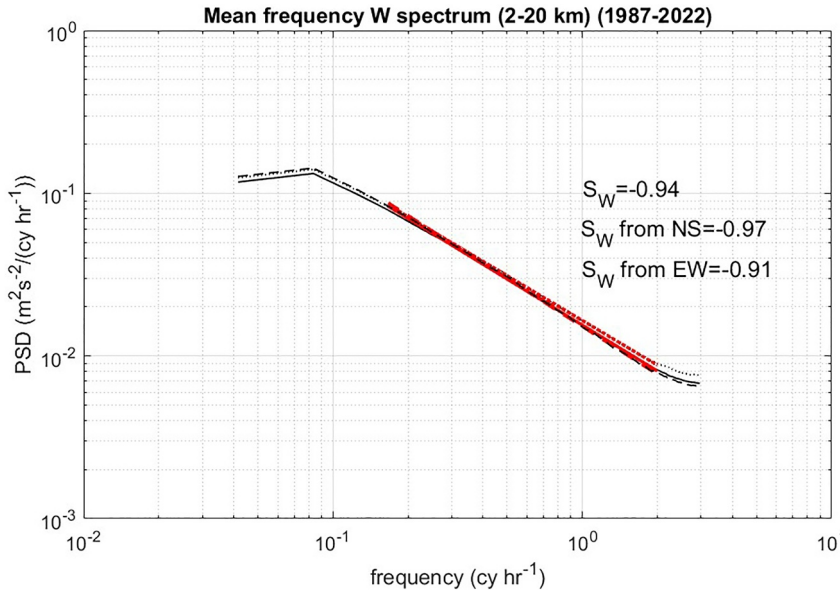

Figure 5. Mean frequency spectrum of the vertical velocity measured from the vertical beam and reconstructed from the N-S and E-W beams for the period (1987–2022) and for the height range [2–20 km]. The red lines show the linear fit for [0.5–6.0 hr].

MV give similar results. ERRS is positive (i.e., shallower slopes are estimated) and increases almost linearly with the percentage of missing data (∼0.08 per 10%). For example, a randomly distributed data gap of 15% (here ∼21 data among 144) is responsible for a statistical error in S_W of ∼0.13 (i.e., a shallower slope, e.g., −0.87 instead of −1) for the three methods. FFT-LI produces a negative ERRS (i.e., a steeper slope) of amplitude almost identical to the other methods. However, ERRS for RMD should be considered as maximum errors. As the missing data are often a mixture of CMD and RMD, we can expect |ERRS| much less than 0.13 for 15% of missing data.

Overall, ERRV is negative (i.e., the variance is underestimated) for all methods. The curves intersect at different % missing data values, making it difficult to summarize the results. Only LS performs well with negligible ERRV up to ∼15% of missing data for both RMD and CMD. Next comes FFT-LI with |ERRV| < 3% for RMD and |ERRV| < 15% up to ∼15% of missing data. Finally, FFT-MV and DCDFT give a linear decrease in ERRV of 1% per % of missing data at least up to 15%.

As a result, the best estimator for our present purposes seems to be LS. However, all the methods can be used with a maximum of 15% missing data to avoid a maximum error of +0.13 on S_W and 0%–15% on the variance. When averaging over hundreds of spectra calculated from time series of (85–100) % occupancy, the actual |ERRS| (|ERRV|) should be well below 0.13 (15%) for all the methods. We expect that the climatological values of S_W and variances are mainly influenced by other factors.

For measured and synthetic radar data, Zhan et al. (1996) showed that LS does not perform well for horizontal winds and that FFT-LI produces the best performance for the spectral slope and variance. After the submission of this paper, we found that LS, DCDFT, and FFT-MV produce similar biases and confirm the best performance of FFT-LI for horizontal winds (not shown). Although the low-frequency part of the spectra is relatively spared by missing data effects, the high-frequency part is severely biased so that the magnitude of S_W is decreased (the slopes are shallower). The description of our results will be presented in greater detail in a later work combining the analysis of vertical and horizontal winds.

4. Results

4.1. Mean Frequency Spectra of W

Figure 5 shows the (arithmetic) mean of the frequency spectra of W, W_{NS} and W_{EW} for all heights (2.025–19.875 km) and months combined (1987–2022) that meet the criteria defined in Section 3. Here, we used the FFT-

21698996, 2024, 23, Downloaded from https://agupubs.onlinelibrary.wiley.com/doi/10.1029/2024JD041677 by Cochrane Japan, Wiley Online Library on [19/01/2025]. See the Terms and Conditions (https://onlinelibrary.wiley.com/terms-and-conditions) on Wiley Online Library for rules of use; OA articles are governed by the applicable Creative Commons License

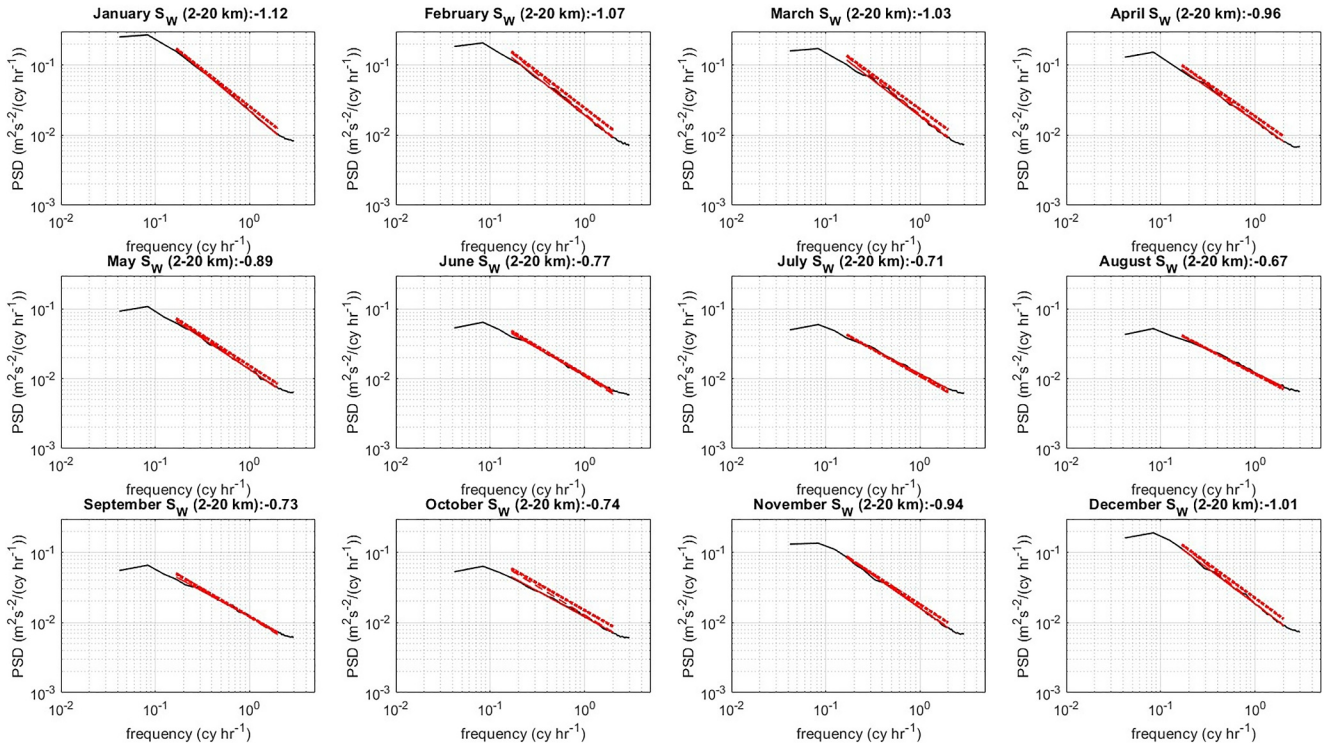

Figure 6. Same as Figure 5 but for each month. The red solid, dashed, and dotted red lines show the linear fit for [0.5–6.0 hr] and for W, W_{NS} and W_{EW}. The W_{NS} and W_{EW} are not shown for readability reasons. The values of S_W are given in the title for each month.

MV method. The number of averaged spectra is 321,539, 230,590, and 214,281 for W, W_{NS} and W_{EW}, respectively. The spectra are very smooth and show a clear linear slope in the band (0.5–6.0 hr). The estimated slopes for W, W_{NS} and W_{EW} are −0.94, −0.97 and −0.91, respectively. They show a small difference, which is unlikely to be due to statistical uncertainty but probably to instrumental bias. They do not show significant differences in levels. A flattening can be observed at the highest frequencies (period less than 30 min) due to the possible effect of missing data with FFT-MV, aliasing, and various noises. For this reason, they were not included in our analysis. The upper limit has been set at 6 hr, the period from which spectral flattening begins for 1-day time series.

Figure 6 shows the same information as Figure 5 but for each month of the year. For readability only, the spectra of W (black) are plotted together with the results of the linear fits for W, W_{NS} and W_{EW} (red). The mean values of S_W for all heights are also given in the title of each panel. The steepest and flattest spectra are observed in January and August, respectively. S_W for W, W_{NS}, and W_{EW} show practically the same evolution with the month (Figure 7). The maximum level difference between the spectra of W , W_{NS}, and W_{EW} is observed in February and October (spectral level for W_{EW} is ∼25% higher than for W). Since the three parameters are expected to represent the same quantity, a (small) contamination must be assumed to explain this difference. Figure 7 shows more clearly the seasonal variation of the mean value of S_W from about −1.1 in winter to about −0.7 in summer, a trend that is almost identical for the three estimates. The difference of 0.03 between S_W for W_{NS} and W in Figure 4 is almost systematic for each month. This characteristic must be independent of the horizontal wind speed, since it varies strongly with the month at the radar site. The seasonal variability of S_W is less important for W_{EW}. Again, since these characteristics are obtained after averaging a large number of spectra over 36 years, they must reveal significant features related to atmospheric properties and/or measurement techniques. In the remainder of this paper, however, we will concentrate on interpreting the characteristics of the spectra of W that are common to the spectra of W, W_{NS} and W_{EW}, since the differences remain very small.

Figures 8a and 8b show the monthly altitude contours of S_W and the corresponding variance (or twice the vertical kinetic energy) in log 10 scale for the period (1987–2022). The seasonal variation of S_W is evident with a weak dependence on altitude except in summer from May to October where the spectra are almost flat above 16 km. This characteristic is clearly associated with a minimum of variance. It is similar to that described by Ecklund et al. (1985,

21698996, 2024, 23, Downloaded from https://agupubs.onlinelibrary.wiley.com/doi/10.1029/2024JD041677 by Cochrane Japan, Wiley Online Library on [19/01/2025]. See the Terms and Conditions (https://onlinelibrary.wiley.com/terms-and-conditions) on Wiley Online Library for rules of use; OA articles are governed by the applicable Creative Commons License

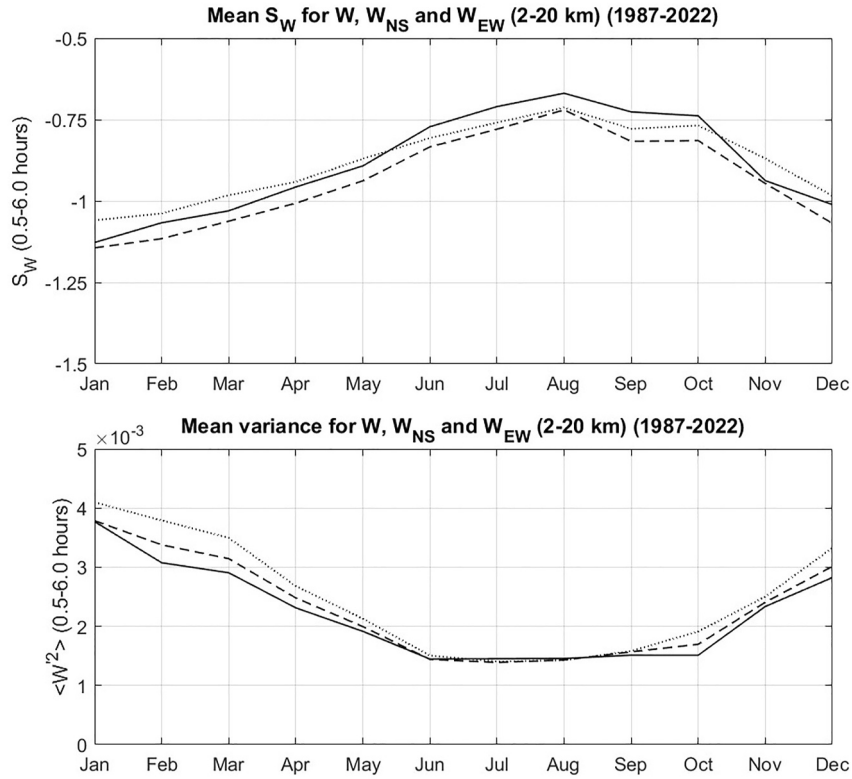

Figure 7. (Top) Monthly means of S_W for W, W_{NS}, W_{EW} for the range of [0.5–6.0 hr] and in the height range [2–20 km] for the period 1987–2022. (Bottom) The corresponding variances $\langle w' \rangle^2$.

1986) for "quiet" conditions, which the authors defined as wind speeds of less than 5 ms^{-1} from the surface to 6 km altitude and less than 10 ms^{-1} from 7 to 20 km altitude. The variance is maximum in winter (DJF) above 12 km altitude and below 4 km altitude in winter and spring. Smaller values of variance are observed in summer below 12 km altitude. There is no perfect correspondence between the variations of S_W and the variance, as the variance shows a minimum between 6 and 8 km altitude in winter, whereas S_W is relatively independent of altitude.

As will be shown later, the flat spectra of W above 16 km in summer are clearly associated with weak horizontal winds (less than ∼10 ms^{-1}), for which the Doppler shifting effect on gravity wave spectra is expected to be minimal (e.g., Fritts & VanZandt, 1987; Scheffler & Liu, 1985, 1986). The Doppler shift due to the background wind on the intrinsic frequency σ of a wave produces an apparent frequency ω for a fixed observer (e.g., a ground-based radar). This effect is specific to propagating gravity waves and does not apply to 2D stratified turbulence. It redistributes energy not only in the frequency band limited by the inertial and buoyancy frequencies, f and N, for gravity waves but also at higher and lower frequencies by upshifting and downshifting, depending on the relative direction between the background wind and the horizontal wave number vector of the gravity wave. For frequency spectra of horizontal winds, generally characterized by a −5/3 slope, the distortions are expected to be maximal near the inertial frequency f (e.g., Fritts & VanZandt, 1987). Hocking et al. (2021) used this property, among others, to study the relative contribution of internal gravity waves and 2D turbulence. In our case, the inertial period is ∼21 hr at MU radar latitude, and the buoyancy period is ∼10 min in the troposphere and ∼5 min in the stratosphere. Our analysis window (0.5–6.0 hr) does not intersect any of these boundaries. However, we will briefly test the hypothesis that the variations of S_W shown in Figures 5–8 may or may not be due to Doppler shift, and we will examine other effects that may affect S_W in the selected band.

4.2. Doppler Shifting of Frequency Spectra

The effect of horizontal wind advection on a gravity wave spectrum for W can be determined from the knowledge of the intrinsic wave spectrum $E^w(\sigma, \mu)$, where σ is the intrinsic frequency and $\mu = k/k_*$ is the horizontal

21698996, 2024, 23, Downloaded from https://agupubs.onlinelibrary.wiley.com/doi/10.1029/2024JD041677 by Cochrane Japan, Wiley Online Library on [19/01/2025]. See the Terms and Conditions (https://onlinelibrary.wiley.com/terms-and-conditions) on Wiley Online Library for rules of use; OA articles are governed by the applicable Creative Commons License

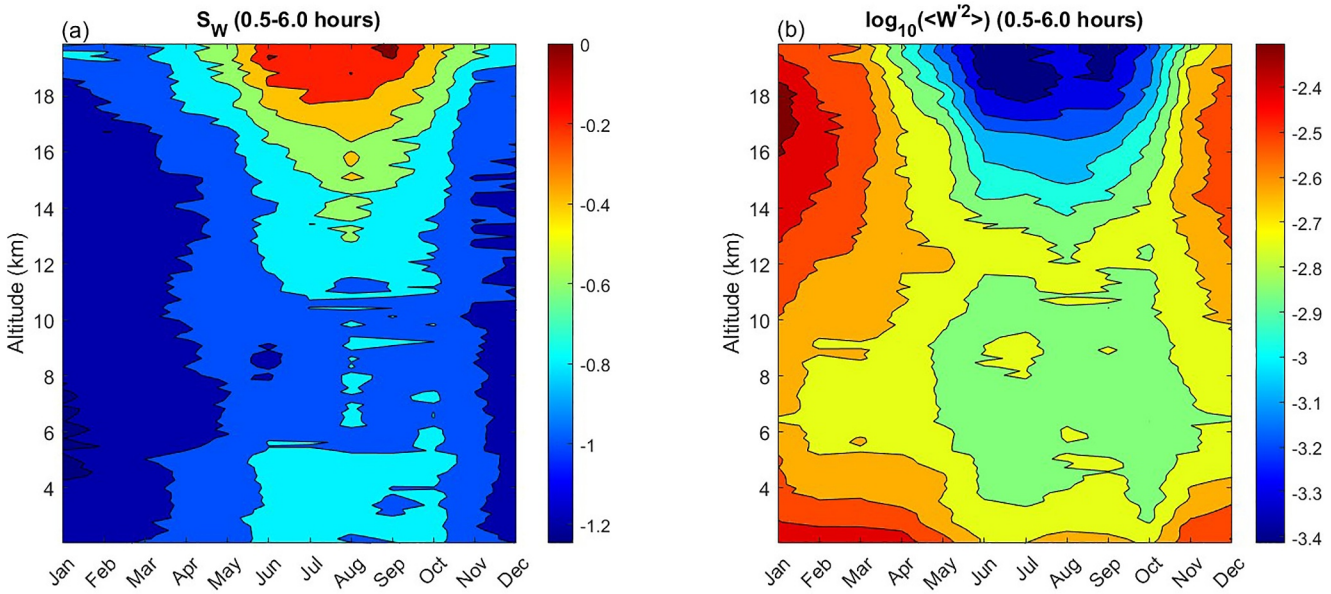

Figure 8. (a) Contour plot of S_W (for the range of periods [0.5–6.0 hr]) versus month and altitude for the period 1987–2022. (b) The corresponding contour plot of $\log_{10}\left(\langle w' \rangle^2\right)$ (for the range of periods [0.5–6.0 hr]).

wavenumber k normalized by a characteristic horizontal wavenumber k_*. A general expression is (e.g., Vanzandt et al., 1991, hereafter referred to as VNG91)

$$E^w(\sigma, \mu) \propto \left(\mu^s/(1+\mu)^{s+t}\right)\sigma^{-p}(\sigma/N)^2\left(1-(f/\sigma)^2\right)^n \quad (1)$$

For $f \le \sigma \le N$. The exponents s, t, and p are determined from observations and $n = 0$ *or* 1 depending on the degree of approximation. Equation 1 is a generalization of Equation 14 of Fritts and VanZandt (1987), hereafter referred to as FV87, who used $s = 0, t = 3$, $p = 2$, and $n = 0$. VanZandt and Fritts (1989) found that $s = 0$ is not physical (unrealistically large vertical fluxes of wave energy) and VNG91 proposed $s = 1, t = 3$, $p = \frac{4}{3}, \frac{5}{3}, 2$, and $n = 1$. Note that $p = 2$ corresponds to a flat intrinsic frequency spectrum (at least for $\sigma \gg f$ when $n = 1$). This is consistent with some theories, for example, the saturated-cascade theory of Dewan (1997). p should vary between 5/3 and 2 (e.g., VanZandt, 1985). We have used $p = 2$, because the results are not strongly dependent on this parameter. The apparent frequency ω is related to σ by

$$\omega = \sigma + kU\cos\varphi = \sigma(1 + \mu u_* \cos\varphi) \quad (2)$$

where U is the mean horizontal background wind speed, φ is the azimuthal angle between $\vec{k}$ and $\vec{U}$ and $u_* = U/c_*$, where $c_* = \sigma/k_*$ is a characteristic horizontal phase velocity. Depending on the sign of $\cos\varphi$, the frequency is shifted up or down. For convenience, FV87 used $\cos\varphi = \pm 1$, that is, all waves propagate in the same vertical plane as $\vec{U}$ and assumed an equipartition of the upshifted and downshifted waves. VNG91 generalized by introducing a uniform distribution of the energy of the upshifted and downshifted waves in each semicircle, but this generalization did not produce substantial differences with the FV87 assumption.

The Doppler-shifted spectra are obtained by replacing μ in Equation 1 by its expression from Equation 2 and integrating Equation 1 from $f \le \sigma \le N$ using the procedure described in Section 3.1 of FV87. They were numerically estimated for (S1): $s = 0, t = 3$, $p = 2$, $n = 0$ (FV87 model) and for (S2): $s = 1, t = 3$, $p = 2$, $n = 1$ assuming $\cos\varphi = \pm 1$ ("linear" azimuthal distribution, VNG91) and for $u_* = 0, 0.8, 2, 5, 10$ and 20. From observations, FV87 argued that u_* should not in principle exceed ~10, but we extended the number to 20 in order to better assess the dependence of the models on this parameter. $u_* = 0$ corresponds to no Doppler shift.

21698996, 2024, 23, Downloaded from https://agupubs.onlinelibrary.wiley.com/doi/10.1029/2024JD041677 by Cochrane Japan, Wiley Online Library on [19/01/2025]. See the Terms and Conditions (https://onlinelibrary.wiley.com/terms-and-conditions) on Wiley Online Library for rules of use; OA articles are governed by the applicable Creative Commons License

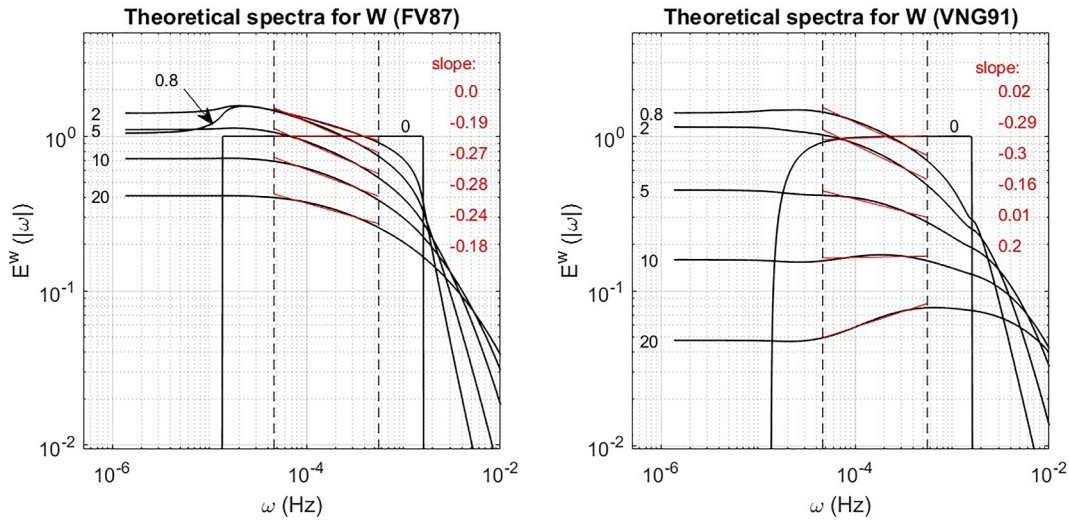

Figure 9. (a) Normalized Doppler shifted spectra E^w given by FV87 (from integration of Equation 1) for $s = 0$, $p = 2$, $t = 3$, $n = 0$, $u_* = 0, 0.8, 2, 5, 10$ and 20, $N^2 = 10^{-4}$ rad^{2}s^{-2} $\left(N = 1.6 \times 10^{-3}\ Hz\right)$, $f = 8.67\ 10^{-5}$ rads^{-1} $\left(f = 1.36\ 10^{-5}\ \text{Hz}\right)$. The dashed vertical lines indicate the range [0.5–6.0 hr] in which the calculated slopes are plotted (red lines) and displayed (red characters). (b) Same as (a) for the VNG91 model for $s = 1$ and $n = 1$. The other parameters are the same. The "linear" azimuthal approximation has been used with equal proportions of the upshifted and downshifted components. See text for further details.

Figure 9 shows the Doppler Shifted (DS) spectra for S1 and S2 cases and for $N^2 = 10^{-4}$ rad^{2}s^{-2} (i.e., $N = 1.60 \times 10^{-3}$ Hz) (troposphere) and $f = 1.36 \times 10^{-5}$ Hz. The total energy is not conserved because the appropriate constants have not been included. Our aim is not to reproduce the characteristics of the DS spectra described by FV87 and VNG91 but to quantify the effect of the Doppler shift on the spectral slopes estimated in the band (0.5–6.0 hr). The DS spectra do not show a linear trend (in log scale) in the band of interest, but the same procedure as for the experimental spectra was used to estimate the spectral slope. It is shown as red lines for each u_* value. Starting from a flat intrinsic frequency spectrum, Doppler shift effects lead to a steepening of the slope, which does not vary much with u_* (and thus with the horizontal wind speed, if we assume $c_*\sim$ constant). The steepening does not exceed ~ -0.2 to -0.3. Considering that the linear azimuthal distribution hypothesis has been used, this steepening should be considered as a maximum value. The maximum is observed around $u_* \sim 5$. Assuming, for example, $c_* = 10$ ms^{-1}, the slope bias would even be reduced if $U > 50$ ms^{-1} (but the fraction of the variance within the selected frequency range decreases monotonically with u_* as shown in Figure 10 of VNG). This effect is even more pronounced for the VNG91 model. The maximum of bias (-0.3) is observed around $u_* \sim 2$ but decreases and is even close to 0 for $u_* = 10$ and becomes positive for $u_* > 10$ ($+0.2$ for $u_* = 20$).

In summary, the Doppler shift effect on S_W cannot exceed a bias of -0.3 in the band (0.5–6.0 hr) for the current models of gravity waves with $p = 0$. Since S_W is in the range $[-0.7;-1.1]$ on average (Figures 5–7), the intrinsic frequency spectra cannot be consistent with the Garrett and Munk/VanZandt model when the observed spectra are corrected for Doppler shift effects. The observed spectra are either affected by other effects or are not well represented by the current analytical models of gravity waves (or both). Figures 10a and b show S_W and variance as a function of U with the mean and median trends (black curves). The color levels indicate the occurrences. The results for S_W are very similar to those shown by Li et al. (2018), although the means are significantly different. S_W increases negatively at a rate of ~ -0.04 per ms^{-1} up to $U = 15 - 20$ ms^{-1} and at a rate of 10 times lower (~ -0.004 per ms^{-1}) between 20 and 70 ms^{-1}. The red curves show the bias in S_W expected from the Doppler shift effect for VNG91 (solid) and FV87 (dashed) for $c_* = 10$ ms^{-1}. VNG91 found $c_* = 6$ ms^{-1} for both the troposphere and stratosphere. The theoretical and observed curves agree only up to 7–8 ms^{-1}. No better agreement was found for other model parameters.

The variance curve (in log scale) is a monotonically increasing function of U. Note that for a given gravity wave spectrum, the variance in a frequency band decreases with U due to Doppler shift effects (see Figure 10 of VNG91).

21698996, 2024, 23, Downloaded from https://agupubs.onlinelibrary.wiley.com/doi/10.1029/2024JD041677 by Cochrane Japan, Wiley Online Library on [19/01/2025]. See the Terms and Conditions (https://onlinelibrary.wiley.com/terms-and-conditions) on Wiley Online Library for rules of use; OA articles are governed by the applicable Creative Commons License

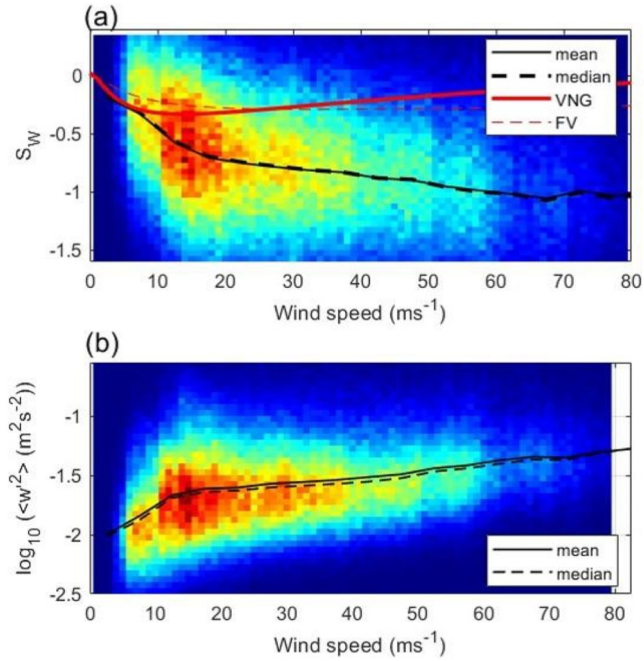

Figure 10. (a) S_W versus 1-day mean horizontal wind speed. The dashed and solid black curves show the median and mean values for bins of 2.5 ms^{-1}. The dashed and solid red curves show the slopes obtained from the FV and VNG models derived from Figure 9 and for a constant characteristic intrinsic horizontal phase speed $c_* = 10$ ms^{-1}. (b) Same as (a) for $\log_{10}(\langle w'^2 \rangle)$.

Therefore, the increase in variance with U shown in Figure 10b should be underestimated. The increase in variance with U cannot be related to the existing model. Dewan (1997) proposed that the intrinsic frequency spectrum for W varies as ε/N^2 where ε is the turbulent kinetic energy dissipation rate. Either the model is inappropriate or the observed spectra are contaminated by contributions other than the gravity waves that depend on U.

4.3. Other Possible Effects Related to Backscattering Mechanisms

To our knowledge, analyses of W frequency spectra with stratosphere-troposphere (ST) radars have not previously considered the possible effects of (a) the increase in the echo power in vertical incidence compared to off-zenith beam directions (called zenith aspect ratio AR) and (b) the power imbalance (PI) between symmetrical beams in oblique incidence. Figures 11a and 11b show S_W versus 1-day mean zenith AR and 1-day mean PI $(P_E - P_W)$ between the east and west beams, respectively. The east and west beams were chosen because they show larger PI values than the north and south beams due to the dominant direction of the eastward winds (and wind shear). The black curves show the mean and median trends. As they are quasi-linear, a linear fit was applied (red lines) for all values of AR and for negative and positive values of PI, since the trends are significantly different depending on the sign of PI. The slopes of the linear fits are referred to here as the "spectral slope trends" T_w^{AR} and T_w^{PI}, respectively. Note that the occurrence of negative PI values is much more important than positive values because the negative values are observed below the jet stream where SNR is statistically higher and data availability is more important (see Figure 2). Note also that the two maxima of occurrence occur around $\sim+1.3$ dB and ~-0.4 dB. The asymmetry in the position of the maxima can be qualitatively explained by the increase of the static stability (and thus AR) in the stratosphere (i.e., ~above 12 km on average).

Figure 11a shows that $T_w^{\mathrm{AR}} = -0.0084\ \mathrm{dB}^{-1}$. This means, for example, that S_W is statistically negatively increased (steeper) by -0.085 for AR = 10 dB compared to AR = 0 dB. $T_w^{\mathrm{PI}} = 0.1831\ \mathrm{dB}^{-1}$ for PI < 0 and $T_w^{\mathrm{PI}} = -0.0325\ \mathrm{dB}^{-1}$ for PI > 0. For PI = −2.5 dB (PI = +2.5 dB), S_W is statistically negatively increased (steeper) by -0.46 (-0.08) compared to PI = 0 dB. These effects are then comparable in amplitude to Doppler shift effect and in the same direction (i.e., steepening of S_W).

Figure 12 shows the scatter plot of AR versus PI. The color levels indicate the horizontal wind shear. The relationship between AR and PI is more complex than AR $= f(\mathrm{PI})$. It has the shape of a pie slice. An increase in

21698996, 2024, 23, Downloaded from https://agupubs.onlinelibrary.wiley.com/doi/10.1029/2024JD041677 by Cochrane Japan, Wiley Online Library on [19/01/2025]. See the Terms and Conditions (https://onlinelibrary.wiley.com/terms-and-conditions) on Wiley Online Library for rules of use; OA articles are governed by the applicable Creative Commons License

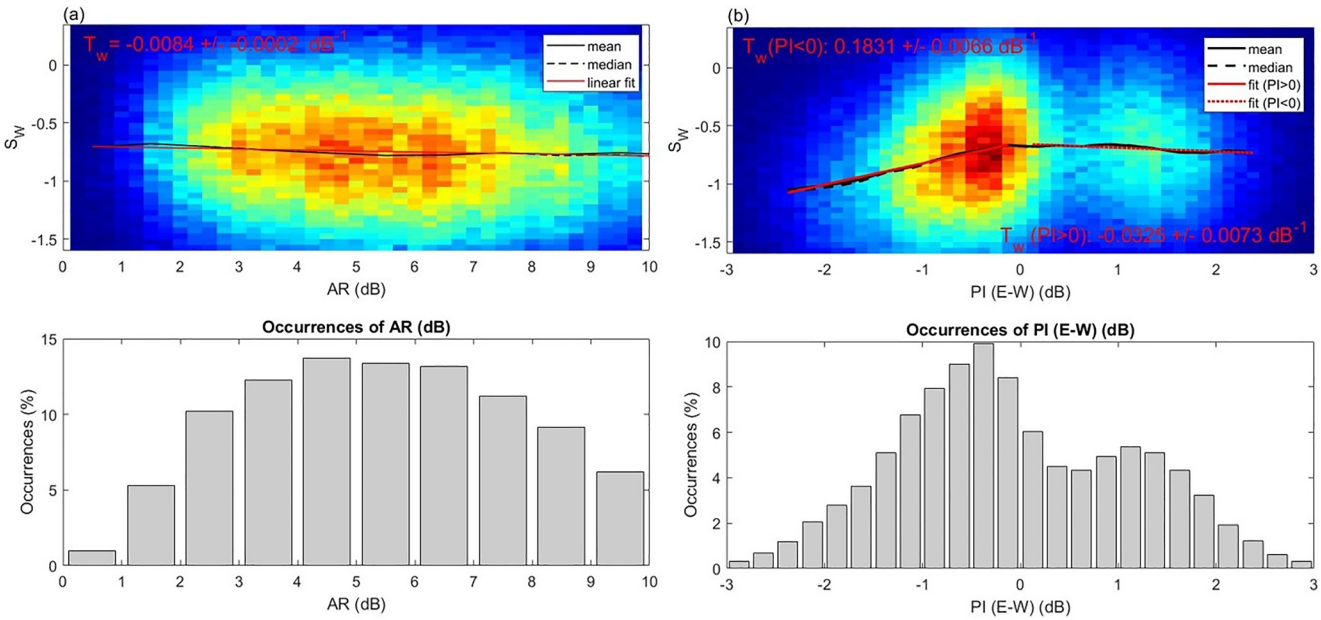

Figure 11. (a, upper panel): S_W versus 1-day mean zenith aspect ratio AR (dB). The dashed and solid black curves show the median and mean values for bins of 1 dB. The red line is the corresponding linear fit and its slope (spectral slope trend) is T_W. (a, bottom panel): Histogram of the 1-day average AR (dB). (b, upper panel) S_W versus 1-day average power imbalance PI (dB) between east and west beams. (b, bottom panel): Histogram of the 1-day average PI (E–W) (dB).

PI is associated with an increase in AR. However, a high AR does not mean a high PI especially when the wind shear is low (blue colors). Therefore, T_W^{AR} includes the effects of PI and T_W^{PI} includes the effects of AR. A more refined description consists in analyzing $T_W^{\mathrm{AR}}(\mathrm{PI})$, that is, T_W^{AR} for fixed values of PI and $T_W^{\mathrm{PI}}(\mathrm{AR})$, that is, T_W^{PI} for fixed values of AR.

The top panel of Figure 13 shows $T_W^{\mathrm{AR}}(\mathrm{PI})$ for $-2.5 \le \mathrm{PI} < +2.5$ dB with a step of 0.3 dB. For example, the first estimate has been obtained using all the values of S_W and AR for $-2.5 \le \mathrm{PI} < -2.2$ dB under the assumption that the range of PI is sufficiently narrow to ignore the effect of its variation. The middle and bottom panels show $T_W^{\mathrm{PI}}(\mathrm{AR})$ for $+3 \le \mathrm{AR} < +10$ dB with a step of 1 dB for $\mathrm{PI} > 0$ and $\mathrm{PI} < 0$, respectively. Results for $\mathrm{AR} < 3$ dB are not available due to insufficient data to estimate T_W^{PI}. The three values of T_w in Figure 11 correspond to the average of the values of the three panels of Figure 13 weighted by the relative number of occurrences of S_W for each interval.

The middle and bottom panels of Figure 13 show that $T_W^{\mathrm{PI}}(\mathrm{AR})$ vary little across the entire range of AR, when $\mathrm{PI} < 0$ and for $\mathrm{AR} > 4$ dB when $\mathrm{PI} > 0$. The positive value for $\mathrm{AR} = 3$ dB is affected by a significant uncertainty and should likely be disregarded. The mean values of $T_W^{\mathrm{PI}}(\mathrm{AR})$ are $+0.174$ for $\mathrm{PI} < 0$ and -0.046 for $\mathrm{PI} > 0$. The top panel shows that $T_W^{\mathrm{AR}}(\mathrm{PI}) \sim 0$ for $-1 < \mathrm{PI} < +1$ dB indicating the absence of significant bias whatever AR. $T_W^{\mathrm{AR}}(\mathrm{PI})$ decreases (i.e., becomes more negative) for $\mathrm{PI} < -1$ dB ($\leftarrow -0.033$) and for $\mathrm{PI} > +1$ dB (~ -0.0085). As (1-day average) AR varies from 0 to ~10 dB, the maximum steepening of S_W is $-0.033 \times 10 \approx -0.33$ for $\mathrm{PI} < -1$ dB and $-0.0085 \times 10 \approx -0.085$ for $\mathrm{PI} > +1$ dB. Compared to the effects of PI, which varies from 0 to 2.5 dB in absolute values, the maximum steepening of S_W is $\sim -0.174 \times 2.5 = -0.43$ for $\mathrm{PI} < 0$ and $\sim -0.046 \times 2.5 \approx -0.12$ for $\mathrm{PI} > 0$, that is, similar values obtained with AR. Therefore, AR and PI effects on S_W seem to be closely related, so it is probably redundant to correct for both AR and PI effects. In the next session, we revise the observed dependence of S_W on U, taking into account the correction for PI effects only.

4.4. Why Does S_W Depend on AR and PI?

The radar echo power imbalance between opposite oblique beams can be due quasi-specular reflectors tilted by the wind shear (tilted layers or tilted facets from corrugated surfaces). The presence of tilted scatterers results in an effective off-vertical beam angle β when the radar beam is directed vertically (Hocking et al., 2016;

21698996, 2024, 23, Downloaded from https://agupubs.onlinelibrary.wiley.com/doi/10.1029/2024JD041677 by Cochrane Japan, Wiley Online Library on [19/01/2025]. See the Terms and Conditions (https://onlinelibrary.wiley.com/terms-and-conditions) on Wiley Online Library for rules of use; OA articles are governed by the applicable Creative Commons License

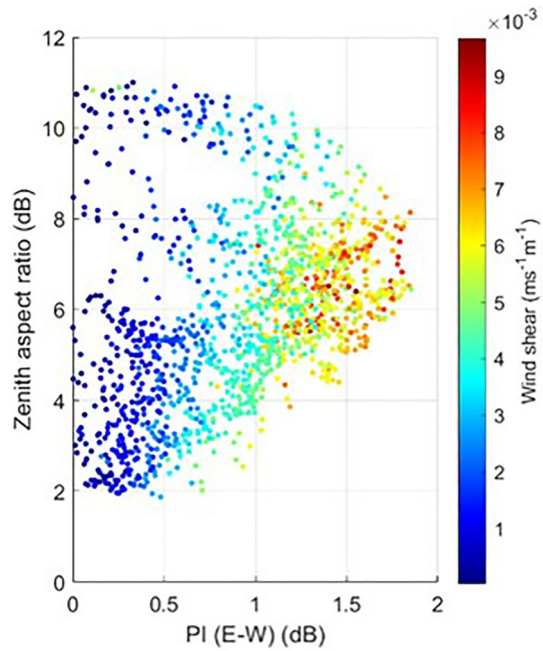

Figure 12. Scatter plot of average zenith aspect ratio AR (dB) versus power imbalance PI $(E - W)$ (dB) and horizontal wind shear (s^{-1}) (color levels).

Muschinski, 1996; Palmer et al., 1991). This angle β depends on the tilt of scatterers, the antenna beam pattern, and the polar diagram of the scatterers (e.g., Hocking et al., 2016). Therefore, the measurements at vertical incidence can be contaminated by the horizontal wind so that:

$$W_{\text{app}} = U \sin \beta + W \cos \beta \tag{3}$$

The spectrum of W_{app} would then be contaminated by the spectrum of U. The strength of the contamination would depend on the ratio R of the total energy (or variance) of the U and W fluctuations and on β. The frequencies affected by this contamination would depend on the slopes of the spectra of U and W. If R is very "large" ("small"), then the contamination is "small" ("large"). Since the spectral slope S_U for U is steeper than S_W ($S_U = S_W + 2$ for theoretical IGWs), the contamination would mainly affect the lowest frequencies of the spectrum. Therefore, the spectral slope for W_{app}, $S_{W\text{app}}$, would be steeper than S_W. In addition, Equation 3 shows that the contamination would increase as β increases. Therefore, $S_{W\text{app}}$ would increase as β increases. Finally, since the increase in β can be a factor in increasing PI, the steepening of $S_{W\text{app}}$ can be associated with an increase in PI, explaining the relationship between the two variables.

If the above hypothesis is relevant, the dependence of S_W on PI would be independent of the sign of PI. However, the dependence of S_W on PI is much smaller when PI > 0 (Figures 11b and 13). Positive (negative) PI are observed above (below) the jet stream, that is, approximately in the stratosphere (troposphere). If R is expected be larger in the stratosphere than in the troposphere (e.g., Murayama et al. (1994) showed this property in summer for the range period [2–21 hr], their Figure 15), the dependence of S_W on PI would be maximum when PI > 0 and minimum when PI < 0. Since this is the opposite of what we observe, we must conclude that the proposed mechanism likely involves other "ingredients" if it is to be a valid explanation. Further studies are needed to clarify this point.

4.5. Relationship Between S_W and Horizontal Winds Speed After PI Effect Correction

Figure 14a is a replication of Figure 8, showing the monthly altitude contour plot of S_W. We have superimposed contours of U (dashed red lines from 6 to 66 ms^{-1}) and three contours of $N^2 = 2 \times 10^{-4}$ $rad^2 s^{-2}$ (white curves) calculated from radiosonde data at Shionomisaki (solid), Tateno (dashed), and Wajima (dotted) meteorological

21698996, 2024, 23, Downloaded from https://agupubs.onlinelibrary.wiley.com/doi/10.1029/2024JD041677 by Cochrane Japan, Wiley Online Library on [19/01/2025]. See the Terms and Conditions (https://onlinelibrary.wiley.com/terms-and-conditions) on Wiley Online Library for rules of use; OA articles are governed by the applicable Creative Commons License

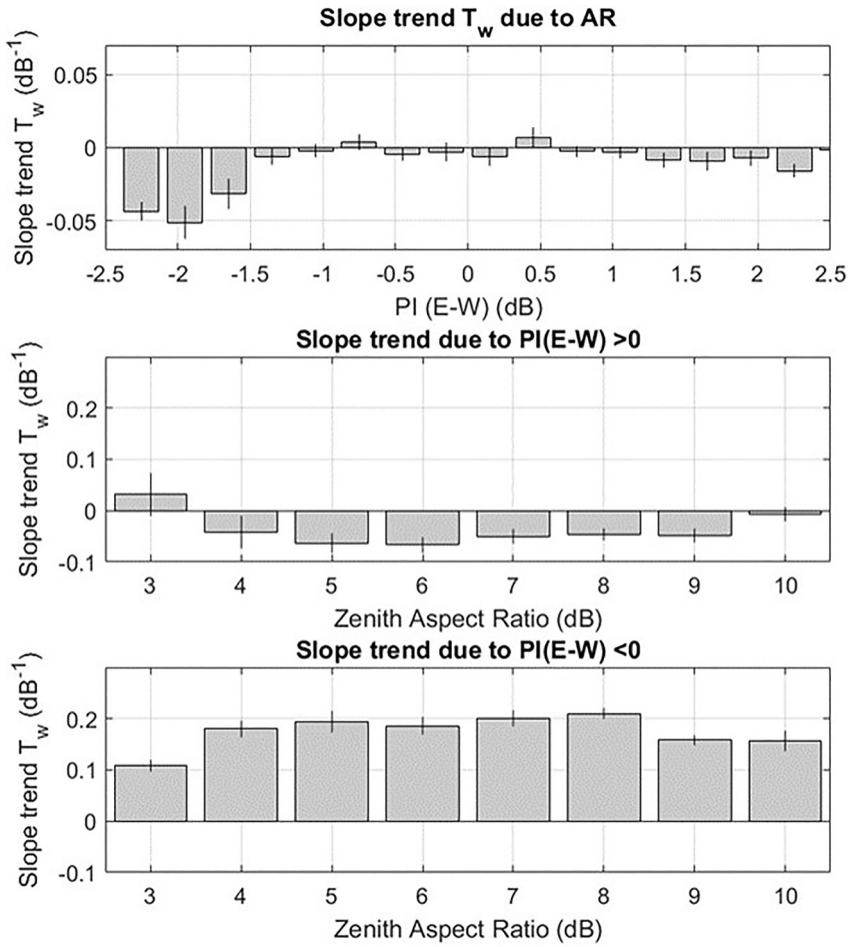

Figure 13. (Top) Spectral slope trend $T_W^{AR}(\mathrm{PI})$ (dB^{-1}) for fixed values of PI from −2.5 dB to +2.5 dB with a step of 0.3 dB. (Middle) $T_W^{PI}(\mathrm{AR})$ for PI > 0 for fixed values of AR from 3 to 10 dB with a step of 1 dB. (Bottom) Same as middle panel for PI < 0. The vertical black segments show uncertainty on T_W of the linear fit.

stations for the whole period (1987–2022). The three curves are very similar. Since the three stations form a triangle around the MU radar site, the height of $N^2 = 2 \times 10^{-4}$ rad^{2}s^{-2} can be used as a proxy for the tropopause height above the MU radar site. Figure 14b shows the same information as Figure 14a but with S_W corrected for PI effects using the values of T_W shown in Figure 11b. This correction reinforces the trends revealed by Figure 8. Below the height of $N^2 = 2 \times 10^{-4}$ rad^{2}s^{-2}, that is, in the troposphere, S_W does not vary much: S_W shows a wide maximum below 6 km in summer and a maximum in the whole troposphere in October but the seasonal dependence has been reduced. Therefore, a large part of the seasonal dependence of S_W in the troposphere shown in Figure 8a should be the result of the seasonal dependence of PI. This is described more quantitatively in Figure 15a. The figure shows the histograms of S_W before and after correction for the PI effect in the troposphere ($N^2 < 2 \times 10^{-4}$ rad^{2}s^{-2}). The initial distribution is asymmetric with respect to a maximum of −0.8 but an average of −0.91. The corrected S_W shows a much narrower distribution centered around −0.78 suggesting that S_W should not vary much with months (±0.1) despite the large seasonal variations of U. In the stratosphere ($N^2 > 2 \times 10^{-4}$ rad^{2}s^{-2}), the effect of the PI correction is less important because PI > 0 (see also Figure 15b). However, the isolines of S_W and U above 12 km appear even more parallel after correction for the PI effect. This is particularly noticeable in the summer when S_W becomes flatter.

Figure 16 shows the relationship between S_W and U in the troposphere and stratosphere. The scatter plot of S_W versus U in the stratosphere shows a clear exponential relationship between the two parameters (Figure 16a). S_W goes to 0 when U is minimal ($U_{\min}$ ~3.5 ms^{-1}) and goes to ~− 1.1 when U is large (>60 ms^{-1}). Contrary to the literature, we were probably able to observe this feature because the jet stream over Japan is very intense in winter

21698996, 2024, 23, Downloaded from https://agupubs.onlinelibrary.wiley.com/doi/10.1029/2024JD041677 by Cochrane Japan, Wiley Online Library on [19/01/2025]. See the Terms and Conditions (https://onlinelibrary.wiley.com/terms-and-conditions) on Wiley Online Library for rules of use; OA articles are governed by the applicable Creative Commons License

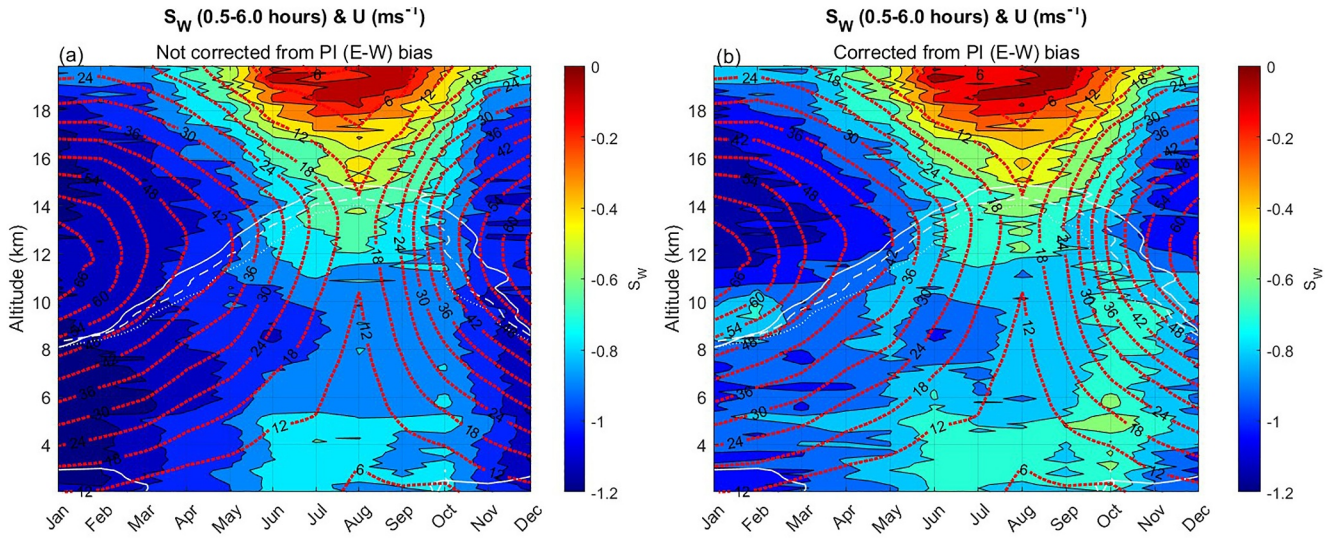

Figure 14. (a) Same as Figure 8a with contour plots of horizontal winds (ms^{-1}) (dotted red) and monthly mean $N^2 = 2 \times 10^{-4}$ rad^2s^{-2} (white) estimated from radiosonde data collected for the period 1987–2022 at three stations around MU Shigaraki Observatory: Shionomisaki (solid), Tateno (dashed), and Wajima (dotted). (b) Same as (a) but after slope corrections for bias associated with PI (E–W) (see Figure 11b).

and very weak in summer. Figure 16b shows the scatter plot of S_W versus $\ln(U - U_{\min})$ and the color levels show N^2. The correlation coefficient between S_W and $\ln(U - U_{\min})$ is -0.91. The linear regression gives a slope of $\alpha = -0.27$ but it is highly dependent on the choice of $U_{\min}$. Therefore, the value of α is uncertain, but the experimental data in the stratosphere clearly show apparent frequency spectra of the form $F^w_{\text{st}}(\omega) \sim \omega^{\alpha \ln(U - U_{\min})}$. When U goes to the minimum as above 16 km in summer, then this empirical expression is consistent with $F^w_{\text{st}}(\omega) \rightarrow \omega^0$. In contrast, the scatter plot of S_W versus $\ln(U)$ in the troposphere (Figure 16c) shows that a weak dependence between two variables. The correlation coefficient is less significant (-0.32) but not negligible, and the regression slope is -0.07 with small variations of the slope around ~ -0.8. Therefore, to a very first approximation, $F^w_{\text{tr}}(\omega) \sim \omega^{-0.8}$ for all seasons.

The largest scatter of S_W versus $\ln(U - U_{\min})$ occurs for the lowest levels of N^2 close to 2×10^{-4} rad^2s^{-2} where the color gradation indicates a dependence of S_W on N^2 (Figure 16b). Therefore, the U dependence of S_W should

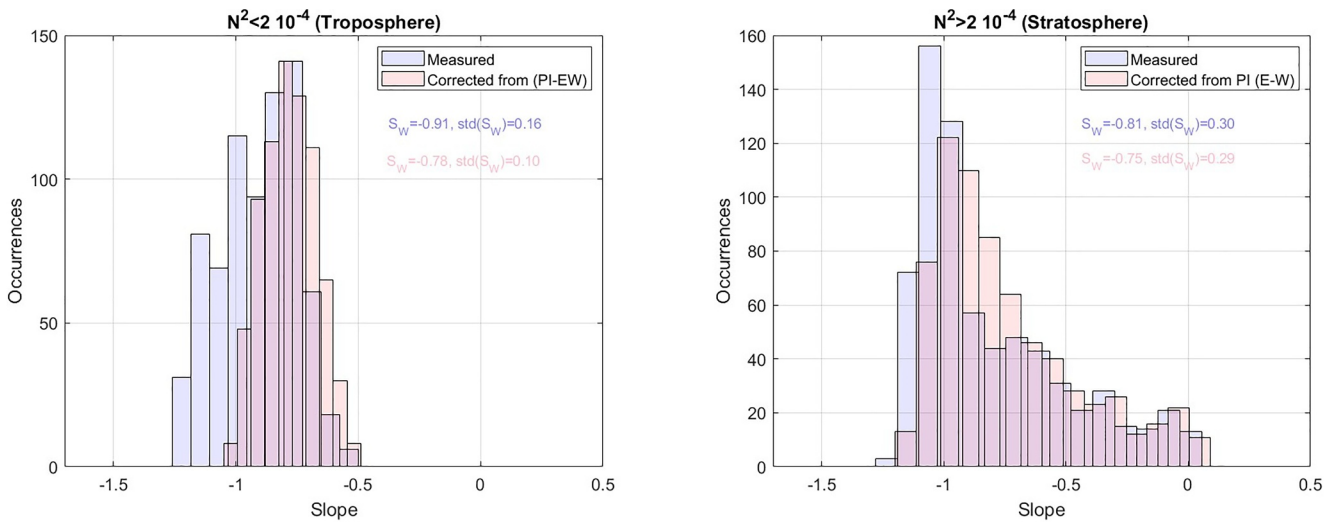

Figure 15. (a) Histogram of S_W for $N^2 < 2 \times 10^{-4}$ rad^2s^{-2} (troposphere) before (blue) and after (pink) corrections from PI($E - W$) biases. (b) Same as (a) for $N^2 > 2 \times 10^{-4}$ rad^2s^{-2} (stratosphere).

21698996, 2024, 23, Downloaded from https://agupubs.onlinelibrary.wiley.com/doi/10.1029/2024JD041677 by Cochrane Japan, Wiley Online Library on [19/01/2025]. See the Terms and Conditions (https://onlinelibrary.wiley.com/terms-and-conditions) on Wiley Online Library for rules of use; OA articles are governed by the applicable Creative Commons License

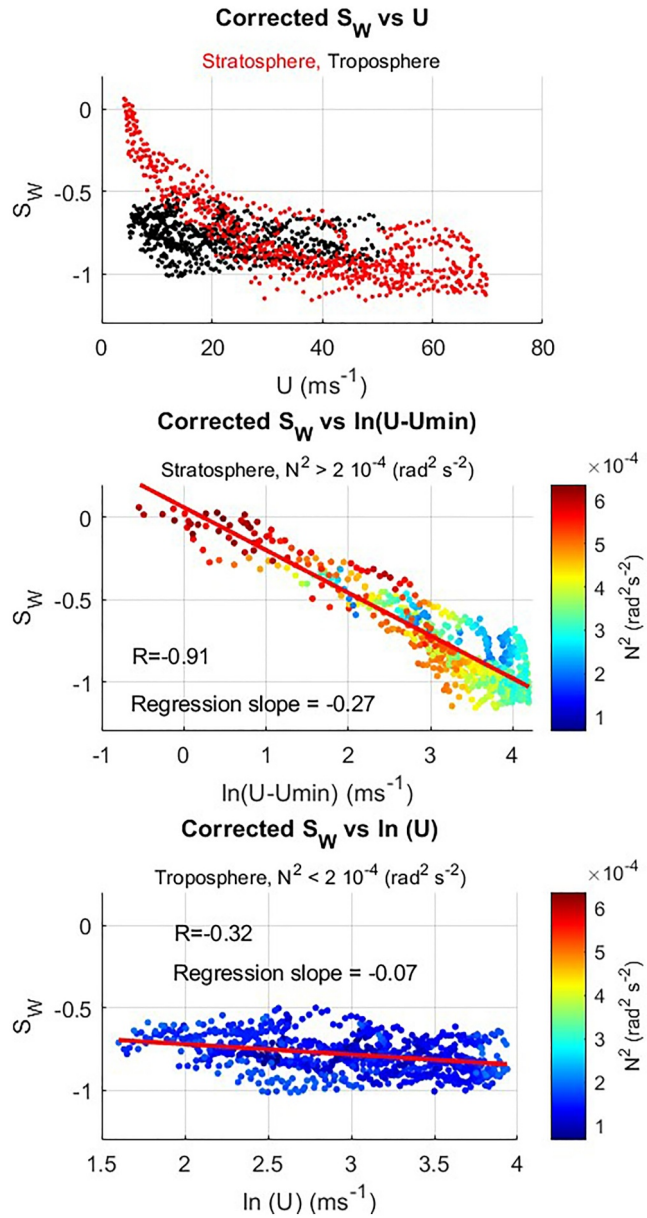

Figure 16. (a) Scatter plot of S_W versus U for $N^2 > 2 \times 10^{-4}$ rad^{2}s^{-2} (stratosphere) and $N^2 < 2 \times 10^{-4}$ rad^{2}s^{-2} (troposphere). (b) Scatter plot of S_W versus $\ln(U - U_{min})$ with $U_{min} = 3.5$ ms^{-1} for $N^2 > 2 \times 10^{-4}$ rad^{2}s^{-2} (stratosphere). (c) Scatter plot of S_W versus $\ln(U)$ for $N^2 < 2 \times 10^{-4}$ rad^{2}s^{-2} (troposphere). The colors indicate N^2 obtained by averaging the monthly mean values estimated at the three meteorological stations.

be established for fixed values of N^2. We analyzed S_W as a function of both U and N^2. The result is shown in Figure 17. First, the distribution below and above $N^2 = 2 \times 10^{-4}$ rad^{2}s^{-2} shows very distinct features as expected from Figures 14 and 16. In the troposphere, S_W weakly depends on U and N^2, but N^2 does not vary much. In the stratosphere, the isolines of S_W are almost "vertical," at least for $U < 30$ ms^{-1}, indicating that S_W is almost independent of N^2. For $U > 40$ ms^{-1}, the isolines of S_W are almost "horizontal," indicating that S_W does not depend on U (consistent with Figure 16a), but on N^2. The figure shows that the largest dependence of S_W in the stratosphere is observed for $N^2 = 3.5 \times 10^{-4}$ rad^{2}s^{-2} and is minimum just above $N^2 = 2 \times 10^{-4}$ rad^{2}s^{-2}. An empirical expression for $F_{st}^{w}(\omega)$ including both U and N^2 is difficult to establish. Data are missing in the upper and lower right corners, because there are no large and small values of N^2 when U is large.

21698996, 2024, 23, Downloaded from https://agupubs.onlinelibrary.wiley.com/doi/10.1029/2024JD041677 by Cochrane Japan, Wiley Online Library on [19/01/2025]. See the Terms and Conditions (https://onlinelibrary.wiley.com/terms-and-conditions) on Wiley Online Library for rules of use; OA articles are governed by the applicable Creative Commons License

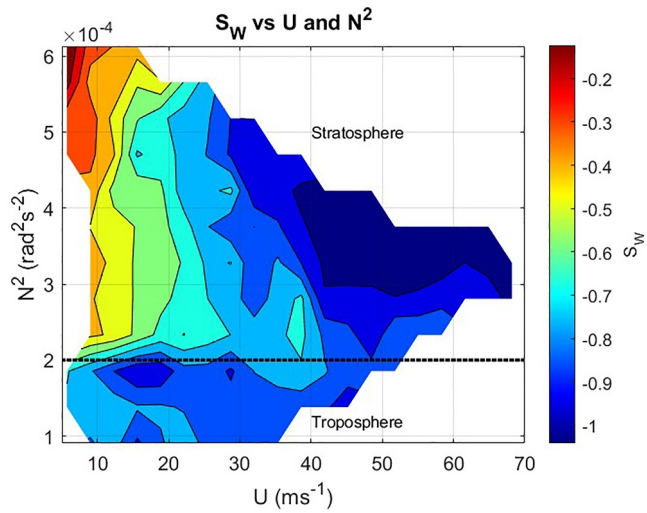

Figure 17. Contour plot of S_W versus U and N^2.

5. Summary and Conclusions

In this paper, we presented a statistical analysis of the frequency spectra of the vertical velocity W in the band [0.5–6 hr] based on data collected with the MU radar from 2.025 to 19.875 km altitude during several days per month over 36 years (1987–2022). First, the performance of the methods used to minimize the effects of missing data on the frequency spectra of W (replacement of missing data or application of spectral estimators dedicated to evenly spaced time series) was clarified. When the data are missing randomly, as is often the case with low SNR, the Lomb-Scargle (LS) estimator, date-compensated discrete Fourier transform (DCDFT), and FFT with missing data replaced by means (FFT-MV) produce shallower slopes in virtually the same way. FFT with missing data replaced by a linear interpolation (FFT-LI) produces steeper slopes with a similar amplitude. However, LS gives the best performance for slopes and variances for occupancy rates of 85% or more when the data are missing randomly or consecutively. Based on these results, we used 1-day time series with a minimum occupancy rate of 85%. This procedure should avoid bias on slopes <<0.1 and on variances (<<15%) for all the tested methods. For the sake of completeness, we analyzed the spectra calculated from W measured directly from the vertical beam and W_{NS} and W_{EW} estimated from the two pairs of oblique beams. The monthly mean slopes of the spectra of W, W_{NS} and W_{EW} show small differences: these differences do not exceed 0.1 when averaged in height. The corresponding variances of W, W_{NS} and W_{EW} in the band [0.5–6 hr] show a maximum of difference in winter (but small, up to ∼20%). In summer, they are almost equal. The mean slopes of the W spectra averaged in height show a seasonal dependence with a minimum of ~ -0.7 in August and a maximum of ~ -1.1 in January. This seasonal dependence can be partly related to a dependence on wind speed U as reported by earlier studies. The spectra are almost flat in summer above 16 km altitude when U is weak $(<10\ \mathrm{ms}^{-1})$ and when the variance is minimal, suggesting a minimum of gravity wave activity. These background conditions correspond to "quiet" conditions for which IGWs, consistent with the Garrett and Munk model, have already been observed (e.g., Ecklund et al., 1986). Comparisons between the measured slopes and the slopes of some Doppler-shifted model spectra of saturated gravity waves (Fritts & VanZandt, 1987; VanZandt et al., 1991) show that the Doppler shift cannot account for the observed dependence on U. In addition, the variance in the [0.5–6.0 hr] band is maximum in winter above 12 km altitude and increases with U. Consequently, if the observations show a dependence of the Eulerian spectra that is qualitatively consistent with the Doppler shift of IGW spectrum models, these models cannot explain the quantitative dependence. In addition, we show that the frequency spectra have very different properties and seasonal variations in the troposphere and in the stratosphere, strengthening the conclusions of previous studies (e.g., Ghosh et al., 2022; Larsen et al., 1987). However, we also found that these results can be affected by measurement biases inherent in the backscattering mechanisms. Indeed, we show that the spectral slopes depend on the zenith aspect ratio and the power imbalance between symmetric oblique beams to an extent similar to the Doppler shift. The contamination of W measurements from horizontal winds due to an effective off-zenith beam-pointing angle

21698996, 2024, 23, Downloaded from https://agupubs.onlinelibrary.wiley.com/doi/10.1029/2024JD041677 by Cochrane Japan, Wiley Online Library on [19/01/2025]. See the Terms and Conditions (https://onlinelibrary.wiley.com/terms-and-conditions) on Wiley Online Library for rules of use; OA articles are governed by the applicable Creative Commons License

21698996, 2024, 23, Downloaded from https://agupubs.onlinelibrary.wiley.com/doi/10.1029/2024JD041677 by Cochrane Japan, Wiley Online Library on [19/01/2025]. See the Terms and Conditions (https://onlinelibrary.wiley.com/terms-and-conditions) on Wiley Online Library for rules of use; OA articles are governed by the applicable Creative Commons License

produced by tilted aspect sensitive scatterers is a plausible hypothesis, but not all properties can be explained even qualitatively. Further studies are required to clarify the cause of these dependencies. After correcting for biases associated with the power imbalance, we found that: (a) the spectral slope in the troposphere (when $N^2 < 2 \times 10^{-4}$ rad^{2}s^{-2}) is indeed almost seasonally invariant (~ -0.8) despite the strong variability of U and (b) the spectral slope is highly variable in the stratosphere (when $N^2 > 2 \times 10^{-4}$ rad^{2}s^{-2}) from ~ 0 to -1.2 and shows a clear exponential dependence with U at least up to 70 ms^{-1}. An empirical expression for the apparent frequency spectra in the stratosphere is $\sim \omega^{\alpha \ln (U - U_{\min})}$ with, for example, $\alpha \sim -0.27$ and $U_{\min} \sim 3.5$ ms^{-1}. The variation of the slope with U can represent a real change in the shape of the intrinsic frequency spectrum. It may also represent the effects of the downshifting of motions at frequencies lower than the inertial frequency (as planetary waves or "external" gravity waves, Hocking et al., 2021), which are not considered in the theoretical models.

Conflict of Interest

The authors declare no conflicts of interest relevant to this study.

Data Availability Statement

The Middle and Upper atmosphere (MU) radar data can be downloaded from the website of the Research Institute for Sustainable humanosphere at https://www.rish.kyoto-u.ac.jp/mu/en/database.html (RISH, 2024) or via the Inter-university Upper atmosphere Global Observation NETwork http://search.iugonet.org/list.jsp.

Acknowledgments
We thank Toshitaka Tsuda for the fruitful discussions on the topic. We also thank the three anonymous reviewers for their comments and suggestions. *Software:* Figures were made with Matlab version R2023a.s.

References

Dewan, E. (1997). Saturated-cascade similitude theory of gravity wave spectra. *Journal of Geophysical Research*, *102*(29), 799–29817. https://doi.org/10.1029/97JD02151

Ecklund, W. L., Balsley, B. B., Carter, D. A., Riddle, A. C., Crochet, M., & Garello, R. (1985). Observations of vertical motions in the troposphere and lower stratosphere using three closely spaced ST radars. *Radio Science*, *20*(6), 1196–1206. https://doi.org/10.1029/RS020i006p01196

Ecklund, W. L., Gage, K. S., Naström, G. D., & Balsley, B. B. (1986). A preliminary climatology of the spectrum of vertical velocity observed by clear-air Doppler radar. *Journal of the Atmospheric Sciences*, *25*(7), 885–892. https://doi.org/10.1175/1520-0450(1986)025<0885:APCOTS>2.0.CO;2

Ferraz-Mello, S. (1981). Estimation of periods from unequally spaced observations. *The Astronomical Journal*, *86*(4), 619–624. https://doi.org/10.1086/112924

Fritts, D. C., & VanZandt, T. E. (1987). Effects of Doppler shifting on the frequency spectra of atmospheric gravity waves. *Journal of Geophysical Research*, *98*(D8), 9723–9732. https://doi.org/10.1029/JD092iD08p09723

Fukao, S., Sato, T., Tsuda, T., Kato, S., Wakasugi, K., & Makihira, T. (1985). The MU radar with an active phased array system, 1. Antenna and power amplifiers. *Radio Science*, *20*(6), 1155–1168. https://doi.org/10.1029/RS020i006p01155

Garrett, C., & Munk, W. (1975). Space-time scales of internal waves: A progress report. *Journal of Geophysical Research*, *80*(3), 291–297. https://doi.org/10.1029/JC080i003p00291

Ghosh, P., He, M., Latteck, R., Renwitz, T., Avsarkisov, V., Zecha, M., & Chau, J. L. (2022). Characteristics of frequency-power spectra in the troposphere and lower stratosphere over Andoya (Norway) revealed by MAARSY. *Journal of Geophysical Research*, *127*(13), e2021JD036343. https://doi.org/10.1029/2021JD036343

Hassenpflug, G., Yamamoto, M., Luce, H., & Fukao, S. (2008). Description and demonstration of the new middle and upper atmosphere radar imaging system: 1-D, 2-D, and 3-D imaging of troposphere and stratosphere. *Radio Science*, *43*(2), RS2013. https://doi.org/10.1029/2006RS003603

Hocking, W. K., Dempsey, S., Wright, M., Taylor, P., & Fabry, F. (2021). Studies of relative contributions of internal gravity waves and 2-D turbulence to tropospheric and lower-stratospheric temporal wind spectra measured by a network of VHF wind profiler radars using a decade-long data set in Canada. *Quarterly Journal of the Royal Meteorology Society*, *147*(740), 3735–3758. https://doi.org/10.1002/qj.4152

Hocking, W. K., Röttger, J., Palmer, R. D., Sato, T., & Chilson, P. B. (2016). *Atmospheric radar: Application and science of MST radars in the Earth's mesosphere, stratosphere, troposphere, and weakly ionized regions*. Cambridge University Press. https://doi.org/10.1175/JCLI-D-17-0870.1

Huaman, M. M., & Balsley, B. B. (1996). Long-term average vertical motions observed by VHF wind profilers: The effect of slight antenna-pointing inaccuracies. *Journal of Atmospheric and Oceanic Technology*, *13*(3), 560–569. https://doi.org/10.1175/1520-0426(1996)013<0560:LTAVMO>2.0.CO;2

Larsen, M. F., Röttger, J., & Holden, D. N. (1987). Direct measurements of vertical-velocity power spectra with the Sousy-VHF-Radar wind profiler system. *Journal of the Atmospheric Sciences*, *44*(23), 3442–3448. https://doi.org/10.1175/1520-0469(1987)044<3442:DMOVVP>2.0.CO;2

Larsen, M. F., Woodman, R. F., Sato, T., & Davis, M. K. (1986). Power spectra of vertical velocities in the troposphere and lower stratosphere observed at Arecibo, Puerto Rico. *Journal of the Atmospheric Sciences*, *43*(20), 2230–2240. https://doi.org/10.1175/1520-0469(1986)043<2230:PSOOVI>2.0.CO;2

Li, Q., Rapp, M., Stober, G., & Latteck, R. (2018). High-resolution vertical velocities and their power spectrum observed with the Maarsy radar–Part 1: Frequency spectrum. *Annales Geophysicae*, *36*(2), 577–586. https://doi.org/10.5194/angeo-36-577-2018

Lilly, D. K. (1983). Stratified turbulence and the mesoscale variability of the atmosphere. *Journal of the Atmospheric Sciences*, *40*(3), 749–761. https://doi.org/10.1175/1520-0469(1983)040<0749:STATMV>2.0.CO;2

Lomb, N. R. (1976). Least-squares frequency analysis of unequally spaced data. *Astrophysics and Space Science*, *39*(2), 1841–1854. https://doi.org/10.1076/brhm.30.2.178.1422

Luce, H., Kantha, L., Hashiguchi, H., & Lawrence, D. (2019). Estimation of turbulence parameters in the lower troposphere from ShUREX (2016–2017) UAV data. *Atmosphere*, *10*(7), 384. https://doi.org/10.3390/atmos10070384

Murayama, Y., Tsuda, T., & Fukao, S. (1994). Seasonal variation of gravity wave activity in the lower atmosphere observed with the MU radar. *Journal of Geophysical Research*, *99*(11), 23057–23069. https://doi.org/10.1029/94JD01717

Muschinski, A. (1996). Possible effect of Kelvin-Helmholtz Instability on VHF radar observations of the mean vertical wind. *Journal of Applied Meteorology*, *35*(12), 2210–2217. https://doi.org/10.1175/1520-0450(1996)035<2210:PEOKHI>2.0.CO;2

Muschinski, A., Chilson, P. B., Palmer, R. D., Hooper, D. A., Schmidt, G., & Steinhagen, H. (2001). Boundary-layer convection and diurnal variation of vertical-velocity characteristics in the free troposphere. *Quarterly Journal of the Royal Meteorology Society*, *127*(572), 423–433. https://doi.org/10.1002/qj.49712757210

Palmer, R. D., Larsen, M. F., Woodman, R. F., Fukao, S., Yamamoto, M., Tsuda, T., & Kato, S. (1991). VHF radar interferometry measurements of vertical velocity and the effects of tilted refractivity surfaces on standard Doppler mea-surements. *Radio Science*, *86*, 417–427. https://doi.org/10.1029/91RS00006

RISH. (2024). MU radar observation data [Dataset]. RISH (Research Institute for Sustainable Humanosphere). https://www.rish.kyoto-u.ac.jp/mu/data/mudata.2024.html

Scargle, J. D. (1982). Studies in astronomical time series analysis. II. Statistical aspects of spectral analysis of unequally spaced data. *The Astrophysical Journal*, *302*, 757–763. https://adsabs.harvard.edu/full/1982ApJ.263.835S7

Scheffler, A., & Liu, C. H. (1986). The effects of Doppler shift on gravity wave spectra observed by MST radar. *Journal of Atmospheric and Terrestrial Physics*, *48*(11), 1225–1231. https://doi.org/10.1016/0021-9169(86)90041-3

Scheffler, A. O., & Liu, C. H. (1985). On observation of gravity wave spectra in the atmosphere by using MST radars. *Radio Science*, *20*(6), 1309–1322. https://doi.org/10.1029/RS020i006p01309

VanZandt, T. E. (1982). A universal spectrum of buoyancy waves in the atmosphere. *Geophysical Research Letters*, *9*(5), 575–578. https://doi.org/10.1029/GL009i005p00575

VanZandt, T. E. (1985). A model for gravity wave spectra observed by Doppler sounding systems. *Radio Science*, *20*(6), 1323–1330. https://doi.org/10.1029/RS020i006p01323

VanZandt, T. E., & Fritts, D. C. (1989). A theory of enhanced saturation of the gravity wave spectrum due to increases in atmospheric stability. *Pure and Applied Geophysics*, *130*(2–3), 399–420. https://doi.org/10.1007/BF00874466

VanZandt, T. E., Nastrom, G. D., & Green, J. L. (1991). Frequency spectra of vertical velocity from Flatland VHF radar data. *Journal of Geophysical Research*, *96*(D2), 2845–2855. https://doi.org/10.1029/90JD02220

Wehr, T., Kubota, T., Tzeremes, G., Wallace, K., Nakatsuka, H., Ohno, Y., et al. (2023). The EarthCARE mission – Science and system overview. *Atmospheric Measurement Techniques*, *16*(15), 3581–3608. https://doi.org/10.5194/amt-16-3581-2023

Yamamoto, Y., Tsuda, T., & Adachi, T. (1996). Frequency spectra of wind velocity and temperature fluctuations observed with the MU radar-RASS. *Geophysical Research Letters*, *23*(24), 3647–3650. https://doi.org/10.1029/96GL03374

Zhan, Q., Manson, A. H., & Meek, C. E. (1996). The impact of gaps and spectral methods on the spectral slope of the middle atmospheric wind. *Journal of Atmospheric and Terrestrial Physics*, *58*(12), 1329–1336. https://doi.org/10.1016/0021-9169(95)00159-X

21698996, 2024, 23, Downloaded from https://agupubs.onlinelibrary.wiley.com/doi/10.1029/2024JD041677 by Cochrane Japan, Wiley Online Library on [19/01/2025]. See the Terms and Conditions (https://onlinelibrary.wiley.com/terms-and-conditions) on Wiley Online Library for rules of use; OA articles are governed by the applicable Creative Commons License